Title

Isotherm, Kinetic, Process Modeling, and Techno-Economic Analysis of a Diamine-Appended Metal–Organic Framework for CO2 Capture Using Fixed Bed Contactors

Journal

Energy & Fuels, 35(7)

ISSN

0887-0624

Authors

Hughes, Ryan
Kotamreddy, Goutham
Ostace, Anca
et al.

Publication Date

2021-04-01

DOI

10.1021/acs.energyfuels.0c04359

Peer reviewed

Isotherm, Kinetic, Process Modeling, and Techno-Economic Analysis of a Diamine-Appended Metal–Organic Framework for CO_2 Capture Using Fixed Bed Contactors

Ryan Hughes[1], Goutham Kotamreddy[1], Anca Ostace[1], Debangsu Bhattacharyya[1*], Rebecca L. Siegelman[2,3], Surya T. Parker[3,4], Stephanie A. Didas[3], Jeffrey R. Long[2,3,4], Benjamin Omell[5], Michael Matuszewski[5]

[1]Department of Chemical and Biomedical Engineering, West Virginia University, Morgantown, WV 26506, USA

[2]Department of Chemistry, University of California, Berkeley, California 94720, USA

[3]Materials Sciences Division, Lawrence Berkeley National Laboratory, Berkeley, California 94720, USA

[4]Department of Chemical and Biomolecular Engineering, University of California, Berkeley, California 94720, USA

[5]National Energy Technology Laboratory, 626 Cochrans Mill Road, Pittsburgh, PA 15236, USA

Abstract

Diamine-appended metal–organic frameworks exhibiting step-shaped CO_2 adsorption are exceptional candidates for energy-efficient carbon capture. However, there are few studies examining their performance in real-world capture scenarios, in part due to the challenge inherent in modeling their CO_2 uptake behavior. Here, we develop a dual-site Sips model to fit experimental CO_2 adsorption data for dmpn–Mg_2(dobpdc) (dmpn = 2,2-dimethyl-1,3-diaminopropane; dobpdc^{4-} = 4,4′-dioxidobiphenyl-3,3′-dicarboxylate) and develop a linear driving force model for the adsorption kinetics based on available experimental data. These models are used to develop a dynamic, fixed bed, non-isothermal contactor model using shaped particles of the material, which is validated with experimental breakthrough data. We also examine the effects of the high heat of adsorption of the material on CO_2 uptake performance and find that heat removal is essential to maximize capture performance. We finally investigate "basic" (no bed cooling during adsorption) and "modified" (bed cooling during adsorption) temperature swing adsorption (TSA) processes using dmpn–Mg_2(dobpdc) and their process economics are compared to a state-of-the-art monoethanolamine (MEA) capture system, with and without heat recovery. In the absence of heat recovery, the adsorbent systems are more costly than established technology. However, with 85% heat recovery, both adsorbent-based TSA processes are projected to cost less than the MEA system. This work highlights that thermal management is vital for implementation of dmpn–Mg_2(dobpdc) as a viable CO_2 capture technology. Investigation of other contactor technologies that can provide unique ways to manage system heat represent promising future areas of study.

Key Words
Metal–organic framework, carbon capture, temperature swing adsorption, techno-economic analysis

* Corresponding Author.

Tel: 1-304-293-9335, E-mail: Debangsu.Bhattacharyya@mail.wvu.edu

1. INTRODUCTION

The earth's average temperature has been steadily rising since the late 1800s, and anthropogenic greenhouse gas emissions represent the largest contributor to this change[1]. In particular, carbon dioxide emissions from fossil fuel combustion processes account for nearly 80% of the increased greenhouse gas emissions in the last 50 years[1]. Electricity generating coal-fired plants have contributed substantially to these emission levels, a trend that is expected to continue in the future[2]. The current leading technology to capture CO_2 from these point sources is post-combustion capture using amine-based solvents, but regeneration of these solutions can require an energy penalty of nearly 30% of the power plant output[2].

In recent years, porous coordination solids known as metal–organic frameworks (MOFs) have emerged as promising candidates for carbon capture[2–4]. Composed of metal ions or clusters connected via organic linkers, these materials possess large internal surface areas and highly tunable pore structures and surface chemistries. In particular, it has been shown that appending alkyldiamines at the open metal sites in the framework Mg_2(dobpdc) (dobpdc^{4-} = 4,4′-dioxidobiphenyl-3,3′-dicarboxylate) results in powerful new adsorbents for CO_2 capture under a range of conditions relevant to coal[5–8] and natural gas flue gas[9,10]. These diamine-appended MOFs exhibit much higher working capacities than traditional adsorbents and have the potential to exhibit lower regeneration energies than both leading amine-based solvents and traditional adsorbents as a result of their step-shaped CO_2 adsorption. This unique behavior arises due to an unprecedented mechanism wherein CO_2 inserts into the metal amine bond to form chains of ammonium carbamate[5] or carbamic acid[11] pairs that propagate down the framework channels. Accordingly, negligible CO_2 uptake occurs until a certain threshold pressure or temperature (under isothermal or isobaric conditions, respectively), beyond which point the material exhibits a sharp increase in gas uptake until it is nearly saturated with CO_2. In addition to this unprecedented adsorption behavior, these diamine-appended MOFs exhibit excellent long-term stability and maintain affinity for CO_2 under humid conditions, both desirable attributes for CO_2 capture[6]. Importantly, it is possible to tune the CO_2 adsorption step pressure or temperature simply by changing the structure of the appended diamine[7]. Many of the diamine-appended frameworks studied to date exhibit a low adsorption step pressure of ~1 mbar of CO_2, however, and this strong adsorption can result in high regeneration temperatures[8]. Recently, the framework dmpn–Mg_2(dobpdc) (dmpn =

2,2-dimethyl-1,3-diaminopropane) was found to exhibit step-shaped adsorption at ~15 mbar CO_2 and 40 °C and nearly complete desorption at 100 °C as well as extended cycling stability under humid conditions. These properties render dmpn–Mg_2(dobpdc) a promising candidate for CO_2 capture from pulverized coal fired power plants, although the performance of this material has yet to be modeled under conditions relevant to practical flue gas capture.

Mathematical models are essential for optimal design of industrial-scale capture systems, however only a few studies to date have examined the performance of any diamine-appended Mg_2(dobpdc) for capture applications, and these studied have focused exclusively on mmen–M_2(dobpdc) (mmen = *N*,*N*′-dimethylethylenediamine). Hefti *et al.*[12] used a weighted dual-site Langmuir equation to accurately model step-shaped CO_2 adsorption in mmen–M_2(dobpdc) (M = Mg, Mn, Fe, Co, or Zn) and to evaluate the performance of these materials in a fixed bed temperature swing adsorption (TSA) process. A simplified fixed-bed model using an equilibrium-based shortcut method and an isothermal adsorption step was also developed to model the TSA process and evaluate important performance indicators, including process energy consumption. In later work by the same researchers[13], a detailed partial differential equation model was used to optimize their TSA process with respect to various performance indicators, using a constant mass transfer coefficient for CO_2 that was estimated using experiments with activated carbons[14,15]. Pai *et al.*[16] used a combination of single- and dual-site Langmuir models to predict adsorption equilibrium in mmen–M_2(dobpdc) (M = Mg, Mn, Fe, Co, or Zn) when implemented in a vacuum swing adsorption process. Here, macropore molecular diffusion was assumed to be the controlling mass transfer mechanism and the properties of a commercial zeolite were used to calculate the mass transfer coefficient. These previous studies laid valuable groundwork for exploring the practical performance of diamine-appended M_2(dobpdc) materials, but given that the structure of the appended diamine can significantly alter the shape of the CO_2 adsorption curves, it is challenging to directly apply existing models to new framework variants such as dmpn–Mg_2(dobpdc). Additionally, the above studies do not use kinetic models that have been developed using experimental data for diamine-appended MOFs, and instead rely on mass transfer coefficients developed using generalized correlations or estimated from experimental data for other solid adsorbents. Finally, there are presently no detailed studies in the literature of the economics of amine-appended MOF use in industrial CO_2 capture. Existing process analyses[12,13,16]

mainly focus on energetics, recovery, and efficiency and do not take into account the size and cost of equipment that is needed to achieve those metrics.

Herein, we use a modified weighted dual-site Langmuir isotherm model and a dual-site Sips isotherm model to fit CO_2 adsorption data for dmpn–Mg_2(dobpdc) for the first time. A kinetic model for CO_2 adsorption in dmpn–Mg_2(dobpdc) is also developed from thermogravimetric analysis data and used with the Sips adsorption model to develop a detailed model of a fixed bed contactor, which is validated using experimental breakthrough data. A cost model is also developed for techno-economic analysis of a TSA process using dmpn–Mg_2(dobpdc) as the CO_2 capture material. Initial case studies of an isothermal and adiabatic reactor are further analyzed to investigate how heat generated during adsorption will affect performance. We also carry out a sensitivity study to analyze the effect of important design variables on the process economics and compare the results to those obtained for the state-of-the-art monoethanolamine (MEA) solvent capture system. Finally, axial temperature and loading profiles and system energetics are presented to elucidate the results of the techno-economic analysis.

2. MODEL DEVELOPMENT

2.1 Adsorption Equilibrium Model for dmpn-Mg_2(dobpdc). To the best of our knowledge, no isotherm model for dmpn–Mg_2(dobpdc) currently exists in the literature. Given the unique step-shaped adsorption exhibited by amine-appended M_2(dobpdc) frameworks, traditional isotherm models are not able to fully describe their CO_2 uptake behavior. However, in some cases these models have been adapted or new models developed to account for the stepped adsorption. In the first study of mmen–M_2(dobpdc), CO_2 uptake was modeled using three separate equations before, at, and after the adsorption step[5], but the discontinuity of this approach renders it unacceptable for use in process modeling and optimization. Notably, the weighted dual-site Langmuir model used by Hefti *et al.*[12] was able to accurately predict the complete adsorption profile for mmen–M_2(dobpdc). Kundu *et al.*[17] presented a model for CO_2 uptake in mmen–M_2(dobpdc) derived from quantum and statistical mechanics that was able to predict the position of the isotherm step but poorly reproduced adsorption behavior after the step. Finally, Pai *et al.*[16] separately modeled chemisorption and physisorption of CO_2 in mmen–M_2(dobpdc) and used both single-site and dual-site Langmuir models to fully describe the adsorption data.

We investigated the potential of multiple models to adequately describe the stepped CO_2 uptake in dmpn–Mg_2(dobpdc), including Langmuir, Freundlich, and Toth equations (see Section 1 of the Supporting Information). None of these traditional approaches were able to describe the experimental data satisfactorily. We therefore turned to a weighted dual-site Langmuir model given in Eq. (1), similar to that developed by Hefti *et al.*[12].

$$q^*_{CO_2} = n_L(p,T)\big(1-\omega(p,T)\big) + n_U(p,T)\omega(p,T) \tag{1}$$

Here, $q^*_{CO_2}$ represents the equilibrium loading of CO_2 predicted by the model, p is the CO_2 pressure, and n_L and n_U describe the lower and upper portions of the isotherm before and after the adsorption step. The term $\omega(P,T)$ (Eq. (5)) is a weighting function that shifts the predicted equilibrium loading from the lower to the upper region of the isotherm model as the pressure increases, which enables the modeling of stepped behavior[12]. While it is difficult to find a rigorous physical interpretation of the weighting function, it helps to retain the characteristics of the underlying isotherm, offer flexibility, and have been used in the literature for modeling complex isotherm characteristics of some MOFs[12,18]. The terms n_L and n_U are given by Eqs. (2) and (3):

$$n_L = \frac{n_L^{\infty} d_L p}{1 + d_L p} + d_B p \tag{2}$$

$$n_U = \frac{n_U^{\infty} d_U p}{1 + d_U p} + d_H p \tag{3}$$

$$d_{\propto} = d_{\propto}^{\infty} \exp\left(\frac{E_{\propto}}{RT}\right); \quad \propto \in [L, B, U, H] \tag{4}$$

$$\omega(P,T) = \left(\frac{\exp\left(\dfrac{\ln(p) - \ln(p_{step}(T))}{\sigma(T)}\right)}{1 + \exp\left(\dfrac{\ln(p) - \ln(p_{step}(T))}{\sigma(T)}\right)} \right)^{\gamma} \tag{5}$$

$$\sigma(T) = X_1 \exp\left(X_2\left(\frac{1}{T_0} - \frac{1}{T}\right)\right) \tag{6}$$

$$p_{step}(T) = p_{step,0} \exp\left(\frac{-H_{step}}{R}\left(\frac{1}{T_0} - \frac{1}{T}\right)\right) \tag{7}$$

We note that in Hefti *et al.*[12], the n_L parameter contains only the first term shown in Eq. (2); however, our initial results with this form showed poor model performance at pressures before

the adsorption step. Accordingly, in this work n_L was altered to include the heuristic linear $d_B p$ term to improve the model, analogous to the form of upper isotherm parameter n_U. In Eq. (5), the parameters p_{step} and γ determine the position of the step and σ determines the step width (here, pressure range). The parameters n_L^{∞}, n_U^{∞}, $d_{\propto}^{\infty}$, $E_{\propto}$, γ, X_1, X_2, p, $P_{step,0}$, and H_{step} (a total of 15 parameters) are determined from fits to the experimental data. All parameters derived from this model are given in Table S2 in the Supporting Information.

Previous characterization of various diamine-appended M_2(dobpdc) frameworks via ^{13}C solid-state NMR spectroscopy[11] revealed that a small amount of CO_2 is physisorbed in the materials in addition to the major chemisorption product. Accordingly, a dual-site Sips isotherm model was also used to model the equilibrium of chemisorbed and physisorbed CO_2 in dmpn–Mg_2(dobpdc). This model is used to predict adsorption in heterogeneous systems and has been used previously to describe CO_2 and methane uptake in Mg_2(dobdc) (dobdc^{4-} = 2,5-dioxido-1,4-benzenedicarboxylate)[19], while a single-site Sips equation with added temperature dependent terms has been used to model adsorption of N_2, methane, ethane, and propane on commercial activated carbons and polyvinyl chloride[20]. The dual-site Sips model used in this work is given in Eqs. (8) and (9) and is a modified version of the model developed by Bao *et al.*[19], with the introduction of temperature dependence in the terms q_{chem}^{∞}, q_{phys}^{∞}, and n_{chem}.

$$q_{CO_2}^{*} = q_{chem}^{*} + q_{phys}^{*} \tag{8}$$

$$q_{CO_2}^{*} = q_{chem}^{\infty}\left[\frac{(b_{chem}p)^{1/n_{chem}}}{1+(b_{chem}p)^{1/n_{chem}}}\right] + q_{phys}^{\infty}\left[\frac{\left(b_{phys}p\right)^{1/n_{phys}}}{1+\left(b_{phys}p\right)^{1/n_{phys}}}\right] \tag{9}$$

Here, $q_{CO_2}^{*}$ is the total CO_2 equilibrium loading predicted by the model, p is the equilibrium pressure, and n_{chem} and n_{phys} are fit parameters that account for surface inhomogeneity[19]. The term n_{chem} varies as a function of temperature according to Eq. (10):

$$n_{chem} = n_{chem,0} exp\left[\frac{E_n}{RT_0}\left(\frac{T_0}{T}-1\right)\right] \tag{10}$$

Here, R is the ideal gas constant, T_0 is a reference temperature (318 K), and $n_{chem,0}$ and E_n are parameters determined from the fit. The terms q_{chem}^{∞} and q_{phys}^{∞} in Eq. (9) describe the maximum loading at chemisorption and physisorption sites, respectively, and are given by:

$$q_{chem}^{\infty} = N_{chem}\left[\frac{exp\left(K_a + {K_b}/{T}\right)}{1 + exp\left(K_a + {K_b}/{T}\right)}\right] \tag{11}$$

$$q_{phys}^{\infty} = N_{phys}\left[\frac{exp\left(K_c + {K_d}/{T}\right)}{1 + exp\left(K_c + {K_d}/{T}\right)}\right] \tag{12}$$

Here, N_{chem} is the diamine loading in the MOF (determined experimentally to be 3.82 mmol/g[8]) and K_a, K_b, K_c, K_d, and N_{phys} are fit parameters. Eq. (11) was first derived for the chemisorption sites under the assumption that there is a 1:1 ratio of diamine to chemisorbed CO_2, and Eq. (12) was adopted for the physisorption sites and is analogous to the form of Eq. (11). Parameters b_{chem} and b_{phys} in Eq. (9) are adsorption equilibrium constants for the two adsorption sites, defined by Eq. (13).

$$b_{\propto} = b_{\propto,0}\exp\left[\frac{Q_{st,\propto}}{RT_0}\left(\frac{T_0}{T} - 1\right)\right], \propto \in [chem, phys] \tag{13}$$

Here, $Q_{st,j}$ are the isosteric heats of adsorption at zero loading[19] at each adsorption site that are also determined from the fit, and R is the ideal gas constant. Overall, the dual-site Sips model has 12 parameters that are estimated using the experimental data. All estimated parameters determined for the Sips model are given in Table S3 in the Supporting Information.

Model parameters were estimated using the 'fmincon' routine in MATLAB, which uses a sequential quadratic programming algorithm to solve the following optimization problem:

$$\min_{\theta} \left(\frac{q^*_{CO_2,exp} - q^*_{CO_2,model}}{q^*_{CO_2,exp}}\right)' \Sigma^{-1} \left(\frac{q^*_{CO_2,exp} - q^*_{CO_2,model}}{q^*_{CO_2,exp}}\right)$$

$$s.t. \tag{14}$$

$$f(\theta) = 0$$
$$g(\theta) \leq 0$$

where $q^*_{CO_2,exp}$ represents the experimental equilibrium loading data, $q^*_{CO_2,model}$ represents the model prediction, θ represents the vector of estimated parameters, and $f(\theta)$ and $g(\theta)$ represent the equality and inequality constraints, respectively. For this problem, the equality constraints consist of the isotherm equations for the model of interest listed above, and the inequality constraints consist of upper and lower bounds for the model parameters. The objective function uses a normalized least squares method with a weighting matrix Σ^{-1}. Because a larger number of experimental data points were available at lower pressures than at higher pressure (e.g., see Fig. 3), a weighted objective function was used where the weight for each data point was set to be inversely proportional to the number of data points that are in the same neighborhood of partial pressure as the data point that is being evaluated. Accordingly, the data were divided up into intervals, or bins, of equal length with respect to partial pressure. The bin size was chosen so that every bin contained at least one data point. The weight of a specific data point is then equal to the inverse of the number of data points in the bin where the data point of interest resides.

2.2 Reaction Kinetics Model. The kinetics of CO_2 adsorption in powdered dmpn–Mg_2(dobpdc) were characterized using thermogravimetric analysis. Time-dependent uptake data were collected at temperatures of 35, 40, 45, and 50 °C using a pure CO_2 gas stream at atmospheric pressure, following the experimental protocol in Martell *et al.*[21]. The total CO_2 adsorption rate was modeled as the sum of the chemisorption and physisorption rates, and a linear driving force was used to model the kinetics as shown in Eqs. (15) through (17).

$$\frac{dq_{CO_2}}{dt} = \frac{dq_{chem}}{dt} + \frac{dq_{phys}}{dt} = k_{chem}(q^*_{chem} - q_{chem}) + k_{phys}(q^*_{phys} - q_{phys}) \tag{15}$$

$$k_{chem} = k_{chem,0} exp\left[\frac{-E_{chem}}{RT_0}\left(\frac{T_0}{T} - 1\right)\right] \tag{16}$$

$$k_{phys} = k_{phys,0} exp\left[\frac{-E_{phys}}{RT_0}\left(\frac{T_0}{T} - 1\right)\right] \tag{17}$$

Here, q_{chem} and q_{phys} are the loadings of the chemisorption and physisorption products, respectively, and q^*_{chem} and q^*_{phys} are the predicted equilibrium loadings as defined above for the dual-site Sips isotherm model. The parameters k_{chem} and k_{phys} are mass transfer coefficients modeled using a standard Arrhenius equation, and $k_{chem,0}$, $k_{phys,0}$, E_{chem}, and E_{phys} are parameters determined from fitting the model to the experimental data. Model parameters were

estimated using the fmincon routine in MATLAB and a sequential quadratic programming algorithm to solve the following optimization problem:

$$\min_{\theta} \left(\frac{q_{CO_2,exp} - q_{CO_2,model}}{q_{CO_2,exp}} \right)' \Sigma^{-1} \left(\frac{q_{CO_2,exp} - q_{CO_2,model}}{q_{CO_2,exp}} \right) \quad (18)$$

s.t.

$$f(\theta) = 0$$
$$g(\theta) \leq 0$$

where $q_{CO_2,exp}$ represents the experimental loading data, $q_{CO_2,model}$ represents the model prediction, θ represents the vector of estimated parameters, and $f(\theta)$ and $g(\theta)$ represent the equality and inequality constraints, respectively. For this problem, the equality constraints consist of the kinetic equations listed above, and the inequality constraints consist of upper and lower bounds for the model parameters.

2.3 Fixed Bed Reactor Model. A first principles fixed bed model that can predict key mass and heat transfer phenomena can be instrumental when attempting to find optimal contactor designs, process parameters, and evaluate process performance. In this work, we modeled an axial-flow fixed bed using Aspen Adsorption V9, which contains a framework that simultaneously solves sets of equations comprising mass, momentum, and energy conservation. For cooling during CO_2 capture and heating during desorption, the fixed bed reactors were modeled with an embedded heat exchanger with a configuration similar to a shell-and-tube heat exchanger. In this configuration, multiple tubes are located inside the reactor, with the heat transfer fluid located in the tube side and the shaped adsorbent particles located in the shell side surrounding the tubes (see Fig. 1). For this work, a reactor is defined as the equipment that contains the bed of adsorbent particles and the embedded heat exchanger. The key assumptions of our model include:

(1) one-dimensional axial variation of the transport variables (i.e., concentration, temperature, velocity, and pressure) and

(2) negligible spatial variation of the temperature within individual particles.

Axial dispersion is neglected since in the velocity range considered in this study and due to the reasonably fast kinetic and mass transfer rates, convective flux is found to be the dominating mechanism. It can be noted that consideration of the axial dispersion term can considerably add to

the computational expense. Several studies were conducted, and it was observed that if axial dispersion is considered, the cycle time differs by less than 0.1% while the CPU time for the simulation increases by more than 20% when compared to the model with no axial dispersion. Therefore, the axial dispersion term is no more considered. The model also accounts for external and internal mass transfer limitations and heat transfer between the gas and solid phase as well as the gas phase and embedded exchanger. The current model considers that CO_2 is the only adsorbed species, and that the presence of O_2, N_2, and H_2O does not affect the adsorption equilibrium or mass transfer of CO_2 given that O_2 and N_2 isotherms for dmpn-Mg_2(dobpdc) show adsorption of these species is negligible while maintaining a high selectivity of CO_2[8], and dry and humid breakthrough data for dmpn–Mg_2(dobpdc) using 15% CO_2 in N_2 are nearly identical[8]. O_2 and N_2 are also likely to have a negligible effect on the purity of the regenerated CO_2 stream. Milner *et al.*[8] show that at compositions typical for coal flue gas, CO_2 will make up greater than 99% of the total adsorbed content of CO_2, O_2, and N_2 based on non-competitive adsorption equilibrium data. The energy released by these species is also expected to be negligible due to the small amounts adsorbed when compared to CO_2. Additionally, although the underlying mechanism of adsorption has been shown to change in the presence of water, the CO_2 capacity remains the same as that under dry conditions[11].

2.3.1 Bulk Gas Phase Species Balance.

$$\varepsilon_b \frac{\partial C_{g,i}}{\partial t} = -\frac{\partial \left(v_g C_{g,i}\right)}{\partial z} - (1-\varepsilon_b)\frac{6k_{f,i}}{d_p}\left(C_{g,i} - C_{surf,i}\right) \tag{19}$$

The gas phase species balance given in Eq. (19) relates the accumulation of gaseous species *i* to the axial convection and also the mass transfer of the gas to the solid phase. In this equation, ε_b represents the voidage in the bed, $C_{g,i}$ represents the bulk gas phase concentration of species *i*, v_g is the superficial gas phase velocity, $k_{f,i}$ is the gas-phase film mass transfer coefficient, d_p is the diameter of the particle, and $C_{surf,i}$ is the concentration of species *i* at the surface of the particle. The difference between the bulk gas phase concentration and the gas phase concentration at the particle surface determines the driving force for gas phase mass transfer.

2.3.2 Mass Transfer. For shaped particles that are used in a fixed bed contactor, the mass transfer mechanisms captured in the kinetic model developed in Section 2.2 will still be present, with the addition of particle diffusion. To account for this additional mechanism, the mass

transfer coefficients used in the fixed bed reactor model include particle diffusion and reaction kinetics. The overall mass transfer resistance from the shaped particles was modeled as the sum of the mass transfer resistances due to macropore particle diffusion[22] and the reaction kinetics for both the chemisorption and physisorption products, as given in Eqs. (20) and (21).

$$\frac{1}{k_{OC}} = \frac{r_p^2}{15\varepsilon_p D_{eff}} + \frac{1}{k_{chem}} \tag{20}$$

$$\frac{1}{k_{OP}} = \frac{r_p^2}{15\varepsilon_p D_{eff}} + \frac{1}{k_{phys}} \tag{21}$$

k_{OC} and k_{OP} are the overall mass transfer coefficients for the physisorbed and chemisorbed products, respectively, and k_{chem} and k_{phys} are defined in Eqs. (16) and (17). D_{eff} is the effective particle diffusion given by:

$$D_{eff} = C_1(T_s)^{0.5} \tag{22}$$

The parameter C_1 encapsulates all particle diffusion mechanisms and is estimated using fixed bed experimental breakthrough data. Additionally, experimental data for parameter estimation of the effective diffusion model is only available for a single temperature, so the model assumes that the effective diffusion will vary with a square root relationship to temperature, which is common for Knudsen type diffusion[23]. These coefficients are then used in a similar linear driving force model which, for clarity, is given in Eq. (23)

$$\frac{dq_{CO_2}}{dt} = \frac{dq_{chem}}{dt} + \frac{dq_{phys}}{dt} = k_{OC}(q^*_{chem} - q_{chem}) + k_{OP}\left(q^*_{phys} - q_{phys}\right) \tag{23}$$

The rate of adsorption/desorption in an adsorbent particle is calculated assuming a linear driving force:

$$R_i = \frac{6k_{f,i}}{d_p}\left(C_{g,i} - C_{surf,i}\right) = \rho_s \frac{\partial q_i}{\partial t} \tag{24}$$

where $k_{f,i}$ is the external (gas film) mass transfer coefficient and $C_{surf,i}$ is the concentration of the gas at the particle surface. Eq. (24) determines $C_{surf,i}$ and accounts for any external mass transfer resistance across the gas film that surrounds the particle.

2.3.4 Gas and Solid Phase Energy Balances. The bulk gas phase energy balance is given in Eq. (25) and relates the change in temperature of the gas to axial heat convection, gas expansion or compression, heat transfer between the gas and solid phase, and heat transfer to the embedded heat exchanger.

$$\varepsilon_b \rho_g C_{v,g} \frac{\partial T_g}{\partial t} = -\rho_g C_{v,g} v_g \frac{\partial T_g}{\partial z} - P \frac{\partial v_g}{\partial z} - (1-\varepsilon_b) a_p h_f (T_g - T_s) - a_{HX} h_{HX} (T_g - T_t) \quad (25)$$

Here, ρ_g is the density of the gas, $C_{v,g}$ is the constant volume heat capacity of the gas, a_p is the specific surface area of the particle, h_f is the heat transfer coefficient for gas and solid phase heat transfer, a_{HX} is the specific surface area for heat transfer with the embedded heat exchanger, h_{HX} is the heat transfer coefficient for the embedded heat exchanger, and T_t is the temperature of the heat exchange medium in the tube.

The solid phase energy balance is given by:

$$\rho_s C_{p,s} \frac{\partial T_s}{\partial t} = \rho_s (-\Delta H_{CO_2}) \frac{dq_{CO_2}}{dt} + a_p h_f (T_g - T_s) \quad (26)$$

The solid phase energy balance relates the change in the temperature of the adsorbent to the heat of adsorption and the heat transfer with the gas phase. Here, ρ_s is the solid density, $C_{p,s}$ is the heat capacity of the solid, and $-\Delta H_{CO_2}$ is the heat of adsorption (see Table 1). Here $-\Delta H_{CO_2}$ is the isosteric heat of adsorption and considered to be constant. A more rigorous approach would be to estimate $-\Delta H_{CO_2}$ as a function of loading and temperature possibly considering a chemistry model.

2.3.5 Embedded Heat Exchanger. The embedded exchanger was designed considering a triangular pitch tube arrangement and the configuration of the exchanger was determined using Eq. (27) and (28) [24].

$$N_t = (CTP) \frac{\pi D_x^2}{4 A_1} \quad (27)$$

$$A_1 = (CL) P_t^2 \quad (28)$$

Here, D_x is the reactor diameter, N_t is the total number of tubes present in the reactor, A_1 is the cross-sectional area of a repeating unit in the reactor that contains a single tube, and P_t is the tube

pitch. CTP and CL are the tube count calculation constant and the tube layout constant, respectively; for one tube pass, CTP = 0.93 and CL = 0.87 for 30 and 60 equilateral tri pitch. Similar configurations can be found in the modeling studies performed by Kim *et al.*[25] and Kotamreddy *et al.*[26].

The heat transfer coefficient between the gas phase and the embedded heat exchanger (h_{HX}) was calculated using correlations from Penny *et al.*[27].

$$Nu_{HX} = \frac{h_{HX} d_t}{k_{eff}} = \left(0.333 + 0.26 Re_{d_t}^{0.533}\right) Pr^{0.33} \left(\frac{d_t}{d_p}\right)^{0.1} \tag{29}$$

Here, Re_{d_t} is the Reynolds number as a function of the heat exchanger tube diameter, d_t:

$$Re_{d_t} = \frac{d_t \rho_g v_g}{\mu_g} \tag{30}$$

The parameter *Pr* is the Prandtl number given by:

$$Pr = \frac{C_{p,g} \mu_g}{k_g} \tag{31}$$

and k_{eff} is the effective thermal conductivity and is a function of the gas thermal conductivity, solid thermal conductivity, and void fraction of the bed.

$$k_{eff} = k_g \left\{ 1 - \sqrt{(1 - \varepsilon_b)} + \frac{2\sqrt{(1 - \varepsilon_b)}}{1 - \lambda\beta} * \left[\frac{(1 - \lambda)\beta}{(1 - \lambda\beta)^2} \ln\left(\frac{1}{\lambda\beta}\right) - \frac{\beta + 1}{2} - \frac{\beta - 1}{1 - \lambda\beta} \right] \right\} \tag{32}$$

$$\lambda = \frac{k_g}{k_s} \tag{33}$$

$$\beta = 1.25 \left[\frac{1 - \varepsilon_b}{\varepsilon_b} \right]^{\frac{10}{9}} \tag{34}$$

2.3.6 Pressure Drop. The pressure drop across the bed was modeled using the Ergun equation[22] (Eq. (35)), which relates the change in pressure to the gas superficial velocity, gas viscosity, as well as other bed properties such as bed voidage and particle diameter.

$$-\frac{\partial P_g}{\partial z} = \frac{150\,\mu_g(1-\varepsilon_b)^2 v_g}{{\varepsilon_b}^3\,{d_p}^2} + \frac{1.75(1-\varepsilon_b)\rho_g|v_g|v_g}{{\varepsilon_b}^3\,d_p} \tag{35}$$

2.3.7 External Heat and Mass Transfer Coefficients. The gas-to-solid heat transfer coefficient was modeled using correlations from Cavenati *et al.*[28] as follows:

$$Nu_f = 2 + 1.1Re^{0.6}Pr^{1/3} = \frac{h_f d_p}{k_g} \tag{36}$$

Similarly, the gas-to-solid mass transfer coefficient is given by:

$$Sh = 2 + 1.1Re^{0.6}Sc^{1/3} = \frac{k_f d_p}{D_g} \tag{37}$$

where *Sc* is the Schmidt number given by:

$$Sc = \frac{\mu_g}{\rho_g D_g} \tag{38}$$

Table 1 lists model parameters that were set as constants. In Milner *et al.*[8], the heat of CO_2 adsorption was found to vary with loading, and the value used in this work is the average heat of adsorption over the entire experimental loading range previously characterized for dmpn–Mg_2(dobpdc). Similarly, the adsorbent heat capacity is based on experimental measurements performed by Milner *et al.*[8]. Model parameters which correspond to the configuration of a shaped particle and its arrangement in a contactor (ε_b, ρ_s, and d_p) are based on the lab-scale fixed-bed experimental setup of Milner *et al.*[8] for compressed, semi-spherical pellets of dmpn–Mg_2(dobpdc). Heat exchanger design variables (d_t and P_t) are similar to the literature and result in a specific heat exchange area of 53 m^2/m^3 which is similar to other studies found in literature[26].

Table 1
Fixed bed reactor model constants.

Parameter	**Value**	**Units**
Heat of CO_2 Adsorption ($\Delta \boldsymbol{H_{CO_2}}$)	−65	[kJ/mol]
Adsorbent Heat Capacity ($\boldsymbol{C_{p,s}}$)	1.457	[kJ·kg^{-1}·K^{-1}]
Bed Voidage ($\boldsymbol{\varepsilon_b}$)	0.68	[m^3 void/m^3 bed]
Density of adsorbent particle ($\boldsymbol{\rho_s}$)	1000	[kg/m^3]
Particle diameter ($\boldsymbol{d_p}$)	525	[µm]
Diameter of heat exchanger tubes ($\boldsymbol{d_t}$)	1	[inches]
Heat exchanger tube pitch ($\boldsymbol{P_t}$)	0.04	[m]

2.4 Post-Combustion CO_2 Capture Process Configuration. A commercial-scale post-combustion temperature swing adsorption (TSA) process model was developed. The cycle begins by flowing the flue gas through a regenerated bed until the bed reaches its breakthrough time. The breakthrough time is defined as the maximum allowable time in which the integral CO_2 slip, or CO_2 that exits the bed, is equal to 10% of the total CO_2 that has been fed to the bed during the current adsorption step (i.e., 90% integral CO_2 capture) [26]. This scenario is described by Eq. (39).

$$0.1 * \int_{t_0}^{t_0+t_b} F_{in}\, y_{CO_2,in} dt = \int_{t_0}^{t_0+t_b} F_{out}\, y_{CO_2,out} dt \quad (39)$$

Once the bed reaches its breakthrough time, it is effectively saturated and therefore the flow of flue gas to the bed is stopped and desorption (regeneration) begins.

Two different configurations for the TSA cycle were considered as shown in Fig. 1. The basic configuration (Fig. 1a) uses condensing steam as the heating medium in the embedded heat exchanger during desorption: steam is introduced into both the embedded exchanger (indirect steam) as well as directly injected into the bed (direct steam). The direct steam provides much less heat than the indirect steam because it is not condensed in the bed, and its primary purpose is to lower the partial pressure of CO_2 in the bed and thereby aid in desorption. The modified configuration (Fig. 1b) utilizes cooling water in the embedded exchanger during the adsorption step to aid in the removal of heat generated upon adsorption and therefore improve bed performance. Note that the use of steam for desorption in this configuration would require that the cooling water first be completely removed from the heat exchanger (for example, using pressured air) to prevent hydraulic shock and potential mechanical damage. In order to avoid the time and cost penalties associated with this added step, hot water (generated in an external heat exchanger by condensing steam) is used as the indirect heating medium during desorption. The use of hot water instead of steam leads to a lower internal heat transfer coefficient for the embedded heat exchanger. However, assuming heuristic heat transfer coefficient values[29] of 850 $W \cdot m^{-2} \cdot K^{-1}$ for condensing steam, 560 $W \cdot m^{-2} \cdot K^{-1}$ for liquid-to-solid, and 60 $W \cdot m^{-2} \cdot K^{-1}$ for gas-to-solid, a quick estimation of the overall heat transfer coefficient ($1/U = 1/h_1 + 1/h_2$) results in 56 and 54 $W \cdot m^{-2} \cdot K^{-1}$, a less than 5% difference and shows that the external heat transfer coefficient between the tube wall and flowing gas is limiting for this system. The driving force for desorption is lower when using hot water, given that the temperature of the water will decrease along its flow direction.

However, this effect can be compensated by increasing the inlet water temperature. Finally, similar to the basic TSA process, direct steam is also introduced into the bed during desorption. For both configurations, the desorption step continues until the average particle loading throughout the bed reaches a desired value. Then, the bed is cooled to the desired initial temperature for the next adsorption step. This adsorption–desorption cycle is repeated several times until the differences between loading and temperature profiles for successive cycles are below a minimum convergence value, achieving a cyclic steady state[30]. The results presented below are cyclic steady state results.

In both models, a sufficient number of adsorbent beds were configured in parallel in order to continuously process large amounts of flue gas, with the assumption that adsorption and desorption are occurring simultaneously in different beds. The total number of beds needed for the TSA process was calculated by solving a scheduling problem that guarantees enough parallel beds are available to continuously process the flue gas. A simplified diagram of the parallel configuration developed for the basic TSA cycle is shown in Fig. 2.

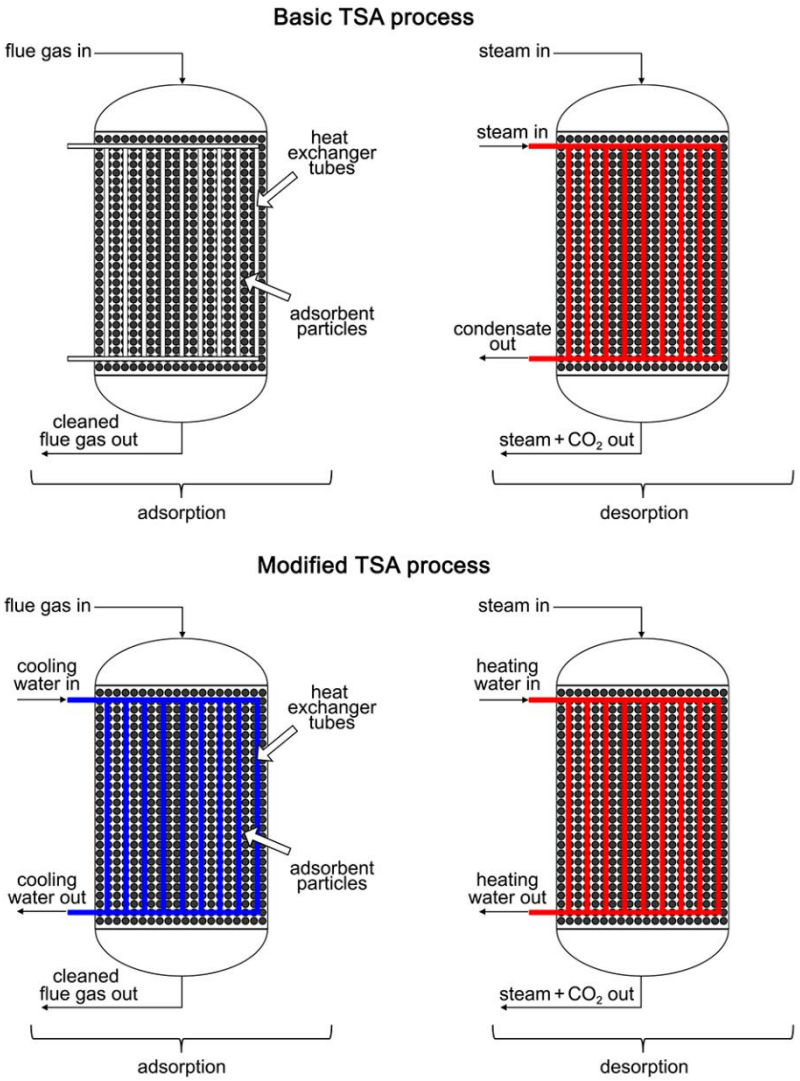

Fig. 1. Configuration steps for the basic TSA process (upper) and the modified TSA process (lower).

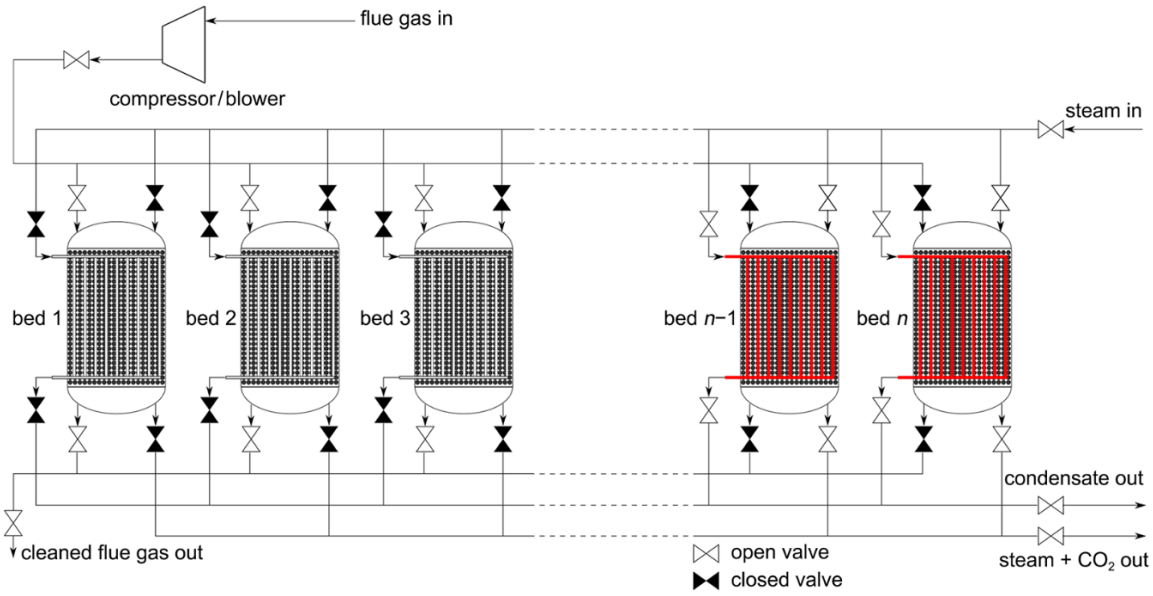

Fig. 2. Simplified diagram of the parallel bed configuration used in modeling the basic TSA cycle. A process that uses *n* beds is shown, with dashed lines representing the possibility of introducing more beds.

2.5 Cost Model. The costs for equipment items used in the process models were determined using the Aspen Process Economic Analyzer (APEA). The reactors and compressors were considered to be the dominant capital costs. The reactors modeled here are very similar in configuration to shell and tube heat exchangers and were priced using APEA. However, the heat transfer area for the reactors considered in the basic and modified processes exceeds the maximum heat transfer area that can be priced in APEA, so the estimated cost for a reactor size of interest was calculated using the following equation[29]:

$$\text{Esimated cost} = \text{Base cost}\left(\frac{\text{required area}}{\text{base area}}\right)^{0.6} \tag{40}$$

Here, the base area is the maximum heat exchange area that can be priced in APEA, the base cost is the cost associated with the base area, and the required area is the area for the reactor of interest. The capital costs considered in this work are bare module costs which are obtained using correlations from Turton *et al.*[29]. The bare module method of costing uses the purchased cost of equipment, which is obtained from APEA and Eq. (40) in this work, and multiplies it by a factor to account for additional expenses due to labor, installation, overhead, and transportation[29]. The capital costs were then amortized over the projected plant life. The discount rate (or interest rate) was assumed to be 10% and the lifespan of the reactors and compressors was set at 10 years. The

other major costs considered in this work are the operating costs due to steam, cooling water, and electricity. These costs are calculated based on the amount used, which is obtained from simulations, and utility prices (see Table S1) obtained from Turton *et al.*[29]. The equivalent annual operating cost (EAOC) was then calculated using Eq. (41).

$$\text{EAOC} = \text{Capital cost}\frac{\text{Discount rate}}{(1-(1+\text{Discount rate})^{-\text{Number of years}})} + \text{Yearly Operating Costs} \qquad (41)$$

We also determined the EAOC of a conventional post-combustion capture system using monoethanolamine (MEA) for comparison. Capital and operating costs for the MEA system were obtained from a study published by the National Energy Technology Laboratory [31].

3. RESULTS AND DISCUSSION

3.1. Isotherm Model Development. As noted earlier, 15 and 12 parameters are estimated for the dual-site Langmuir model and dual-site Sips model, respectively. For estimating these parameters, more than 500 isotherm data showing variation in loading with respect to temperature and pressure have been used. About 100 isotherm data are used for model validation. Various initial guesses were investigated, and the optimizer converged to the same optimal estimates.

Experimental adsorption data for dmpn–Mg_2(dobpdc)[8] and corresponding fits derived using the dual-site Sips and weighted dual-site Langmuir isotherm models are shown in Fig. 3 (see Tables S2 and S3 for the corresponding model parameters and Fig. S9 for residual plots for the isotherm model development). To better visualize the fits to the data, the results shown in Fig. 3 are also presented on a linear scale with respect to partial pressure in Figs. S10 and S11. Both models are able to accurately predict the step locations at all temperatures. The Sips model also provides a good fit to the data before the step transition, but the goodness of the fit diminishes at low temperatures and high pressures. In contrast, the weighted Langmuir model provides a better fit to the data beyond the adsorption step but does not adequately fit the upper region of the adsorption step, particularly at 60 and 75 °C. However, both models show good agreement with the experimental data under conditions relevant to a typical post-combustion TSA process, namely adsorption between 25 and 50 °C at partial pressures between 0.01 and 0.15 bar and desorption between 75 and 120 °C at partial pressures that encompass the range of experimental partial pressures.

During a TSA cycle, the temperatures and partial pressures within the bed can reach values that are between the boundary conditions for adsorption and desorption. Models developed using only experimental data pertaining to those conditions may therefore perform poorly under intermediate conditions. Considering this, additional adsorption data were collected at 80 and 90 °C and used for model validation for both isotherm models (Fig. 4). At 80 °C, the dual-site Sips model predicts a less abrupt step than is present in the experimental data, whereas there is no clear step in the weighted dual-site Langmuir model at the same temperature. At 90 °C, both models predict slightly higher loadings than are observed experimentally, although it is clear that the Sips model performs better overall. Based on the above results and the root mean squared error for each model (Table S4), the dual-site Sips model was selected to predict all subsequent adsorption equilibria., has

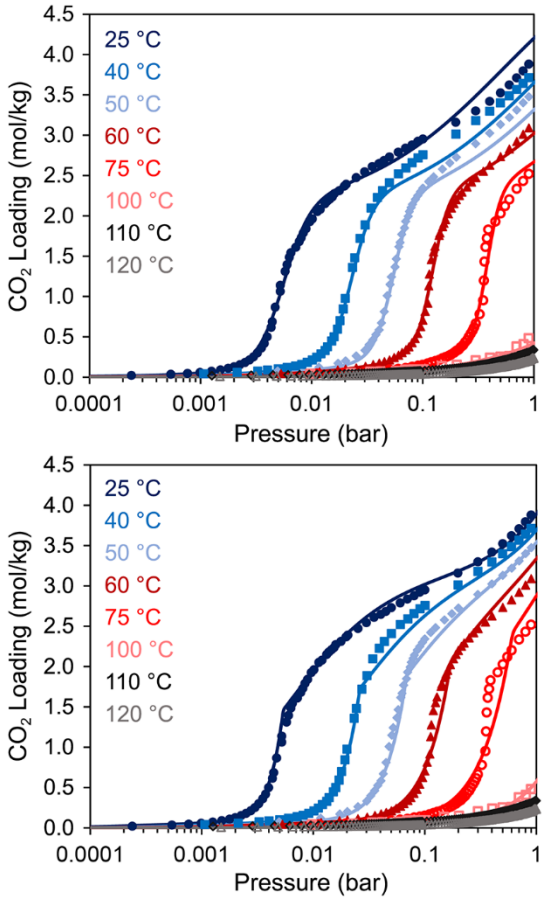

Fig. 3. Experimental CO_2 adsorption isotherms for dmpn–Mg_2(dobpdc) at the indicated temperatures (colored symbols) and fits (colored lines) using a dual-site Sips isotherm model (upper) and a weighted dual-site Langmuir isotherm model (lower).

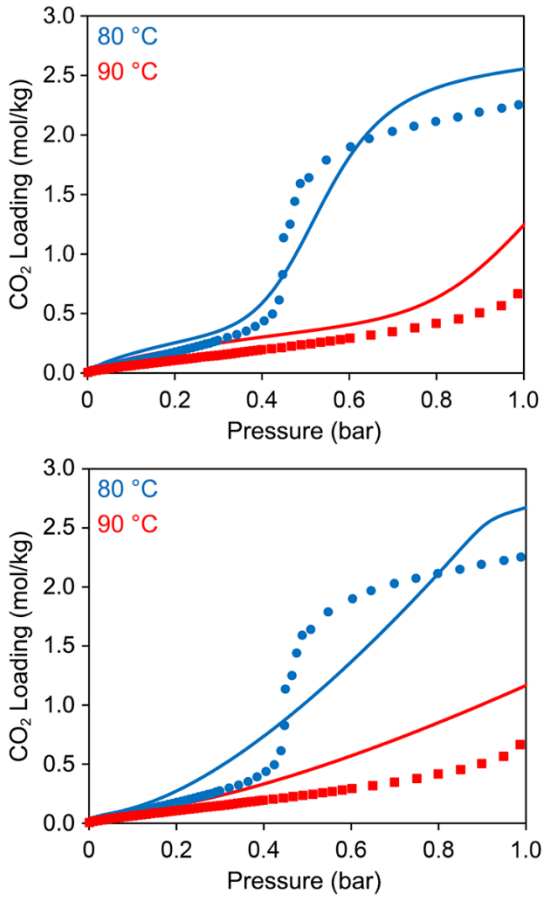

Fig. 4. Model validation results for the dual-site Sips model (upper) and weighted dual-site Langmuir model (lower). Experimental CO_2 adsorption data for dmpn–Mg_2(dobpdc) at 80 and 90 °C are shown as colored symbols and fits to the data are shown as colored lines.

3.2 Kinetic Model Parameter Estimation. Experimental kinetics data for the adsorption of pure CO_2 in dmpn–Mg_2(dobpdc) were used to estimate the parameters for the kinetic model presented in Section 2.2. As seen in Fig. 5, the linear driving force kinetic model is able to accurately describe the kinetics of CO_2 uptake in dmpn–Mg_2(dobpdc).

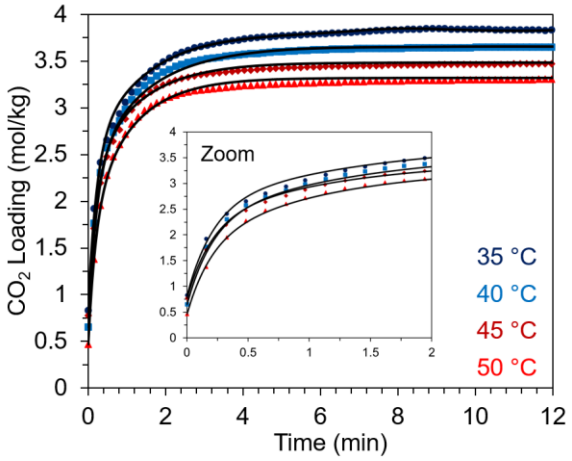

Fig. 5. Experimental data for time-dependent CO_2 adsorption in dmpn−Mg_2(dobdc) (colored symbols) and fits obtained using the linear driving force kinetic model in Section 2.2 (lines), yielding parameters $k_{chem,0}$ = 0.0136 s^{-1} / E_{chem} = 23.21 kJ/mol and $k_{phys,0}$ = 0.0823 s^{-1} / E_{chem} = 7.18 kJ/mol (root mean squared error = 0.025).

3.3 Fixed Bed Model Validation and Parameter Estimation. The fixed bed model presented in Section 2.3 was validated using experimental breakthrough data previously collected for compressed, semi-spherical pellets of dmpn–Mg_2(dobpdc) (see Table 2 for the breakthrough conditions and Milner *et al.*[8] for breakthrough experiment details). It can be noted that the breakthrough experiments are operated isothermally using a water bath, so thermal fronts are expected to be negligible. The isothermal assumption is also corroborated with temperature measurements of the outlet gas which show almost no change (<1 °C) from the design/bed temperature throughout the entire length of the experiment. The effective diffusion, D_{eff}, for the framework particles was calculated using Eq. (22) and a value of C_1 = 4.11×10^{-12} $m^2 \cdot K^{-0.5} \cdot s^{-1}$, which was determined using a least squares estimator and a quasi-Newton based algorithm available in Aspen Adsorption. As shown in Fig. 6, the fixed bed model reproduces both the breakthrough time and the shape of the breakthrough curve, confirming that the bed adsorption capacity and the kinetics of the system under these conditions are well predicted by the model.

Table 2
Experimental breakthrough conditions used to collect data to validate the fixed bed model.

Variable	Value	Units
Bed Length	13.34	[cm]
Bed Diameter	0.46	[cm]
Temperature	40	[°C]
Pressure	1	[bar]
Volumetric Flow Rate	10	[sccm]
y_{CO2}	0.15	[mol fraction]
y_{N2}	0.85	[mol fraction]

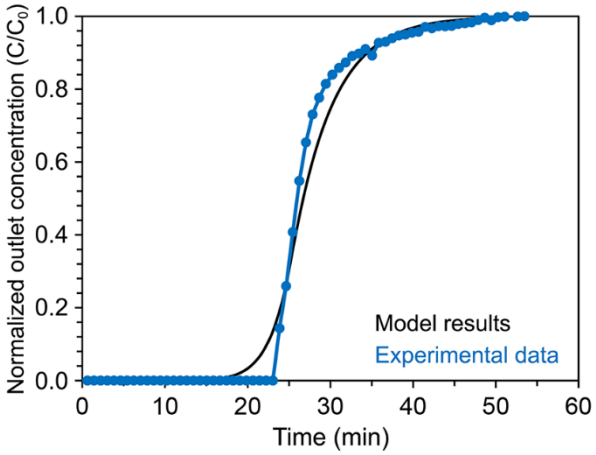

Fig. 6. Comparison of breakthrough model prediction (black trace) and experimental breakthrough data (blue trace). The normalized outlet concentration, C/C_0, represents the concentration of gas phase CO_2 exiting the bed relative to gas phase CO_2 entering the bed (root mean squared error = 0.051).

3.4 Thermal Management Studies. Adsorption of CO_2 in dmpn–Mg_2(dobpdc) is highly exothermic, and the heat released upon CO_2 uptake, coupled with the low material heat capacity, is expected to result in large temperature spikes during the adsorption step. Additionally, CO_2 adsorption isobars for dmpn–Mg_2(dobpdc)[8] indicate that the breakthrough curves will be highly sensitive to temperature. In order to investigate the effects of temperature in greater detail, we simulated isothermal and adiabatic cases using the process conditions outlined in Table 3. The isothermal case study assumes perfect removal of the heat generated during adsorption, whereas no heat removal is considered for the adiabatic case study. As shown in Fig. 7, the breakthrough time in the isothermal scenario is much higher than in the more realistic adiabatic case (80.4 versus

22.7 min, respectively); in other words, achieving perfect heat removal would increase the amount of captured CO_2 by nearly a factor of four. The reduced performance in the adiabatic case can be understood by examining the bed temperature and loading as a function of time (Fig. 8). Here, large temperature spikes of ~40 °C lead to poor CO_2 loading throughout the majority of the bed. For example, at the bed entrance, initial rapid loading of CO_2 causes a temperature spike that results in a much slower continued rate of CO_2 uptake. Incoming flue gas serves to gradually cool the entrance after this spike, but the uptake rate never achieves the initial value. Similarly, temperature spikes at the middle and end of the bed result in a complete plateau in CO_2 uptake at a low loading. These results indicate that efficient heat removal during adsorption would be critical for realizing the potential of dmpn–Mg_2(dobpdc) in a real-world process.

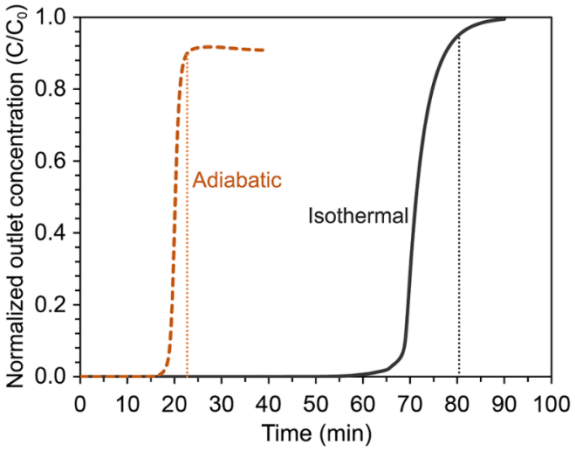

Fig. 7. Modeled breakthrough curves for isothermal and adiabatic case studies discussed in the text. The normalized outlet concentration C/C_0 represents the concentration of gas phase CO_2 exiting the bed relative to gas phase CO_2 entering the bed. Vertical lines correspond to the breakthrough times for each scenario.

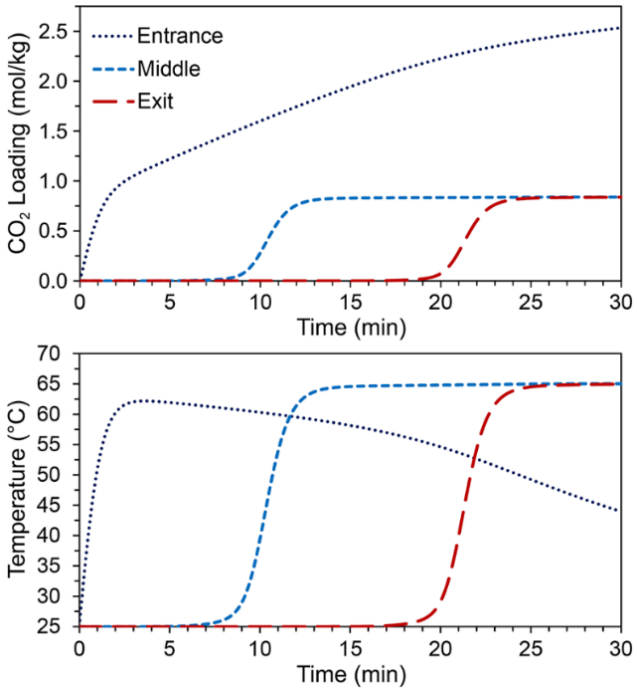

Fig. 8. Dynamic loading (upper) and temperature (lower) profiles at the entrance, middle, and exit of the bed for the adiabatic case study.

Table 3
Process conditions for thermal management case studies.

Variable	Value	Units
Flue Gas Pressure	1.1	[bar]
Flue Gas Temperature	25	[°C]
Flue Gas Flow rate	120	[mol/s]
Flue Gas Composition		
y_{CO2}	0.132	[mol fraction]
y_{H2O}	0.055	[mol fraction]
y_{N2}	0.813	[mol fraction]
Bed Length	10	[m]
Bed Diameter	3	[m]
Initial Bed Temperature	25	[°C]
Initial Bed Loading	0	[mol/kg]

3.5 Techno-Economic Analysis Studies. *3.5.1 Impact of Operating Conditions on Process Economics.* In this section, we present an analysis of process economics sensitivity to the residence time of flue gas in the bed and the bed temperature at the onset of adsorption. Flue gas residence time—which is determined from the volumetric flow of the gas to a single bed, bed length, and bed diameter—directly impacts the number of beds required in the process and

therefore the capital costs. For example, increasing the volumetric flow of the flue gas can decrease the residence time and therefore the number of adsorption beds required to simultaneously process a given amount of flue gas. Conversely, an increase in residence time will generally lead to an increase in the breakthrough time and reduce the cycling rate of the beds but will result in a monotonic increase in the number of required adsorption beds. The importance of temperature and its relation to adsorption capacity and performance has been highlighted in previous sections. It is relevant to note that the pre-adsorption cooling step can add to the total cycle time and increase the number of beds required and therefore the capital costs. However, this time can be considerably reduced by using large flowrate of a gas for cooling like air from the forced draft fan in a pulverized coal plant. In addition, for the modified process, the embedded cooler rapidly cools the sorbent therefore adding an embedded cooler in the pre-adsorption step can further reduce the time for cooling. Therefore, we assume that the cooling time is insignificant when compared to the time required for adsorption/desorption and it is therefore not considered in the cycle time evaluation.

Given the importance of these parameters, we analyzed the sensitivity of the TSA process economics to residence times ranging from 13.9 to 46.5 s at bed temperatures of 25, 35, and 40 °C. For this analysis, it is assumed that the flue gas is available at the same temperature as the initial adsorption temperature. The flue gas conditions used for this analysis correspond to case 11B in the National Energy Technology Laboratory baseline study[31]. The gas was assumed to be generated from a 644 MWe gross power subcritical pulverized coal power plant and to enter the adsorption bed at water saturation for each examined temperature, due to the typical presence of a scrubber before the capture system[31]. Important process variables are shown in Table 4, and the results of the cost analyses are given in Fig. 9 for the basic and modified TSA process scenarios. For the basic process, the EAOC decreases with decreasing residence time down to ~20 s, reflecting the fact that fewer adsorption beds are required to treat a given quantity of flue gas. However, as the residence time decreases, the superficial velocity of the flue gas in the bed correspondingly increases, resulting in a larger pressure drop across the bed (see Eq. (35)). In order to maintain a required outlet pressure of 1 bar, compressors become necessary below a certain residence time to achieve an inlet pressure that is no longer accessible with a traditional blower. As residence times continue to decrease, the operating and capital costs associated with the compressors begin to outweigh the cost savings achieved from reducing the number of adsorption beds, leading to an increase in the EAOC. This balance between adsorbent bed and compressor

cost leads to a minimum EAOC for residence times of 16.1, 18.7, and 18.4 s for bed temperatures of 25, 35, and 40 °C, respectively.

For the modified TSA process, a similar phenomenon is observed, and a minimum in cost occurs at residence times of 32.5 and 31.6 s for bed temperatures of 25 and 35 °C, respectively. In this scenario, the increase in EAOC to the left of the minimum (low residence times) is also associated with the heat generated upon adsorption, which cannot be efficiently removed by the embedded cooler and therefore diminishes the improved adsorption performance that is expected for the modified process. The adsorption performance improves with higher residence times, however, as seen with the basic process, the number of parallel adsorption beds required to process the entire amount of the flue gas increases, driving up the EAOC. Due to the different nature of the systems and improved adsorption performance at higher residence times for the modified process (see Fig. S12), the optimum EAOC for the modified process is at a higher residence time than that for the basic process.

As the initial bed temperature (and correspondingly, the flue gas inlet temperature) is decreased, the EAOC also decreases, given that the framework exhibits a higher loading capacity at lower temperatures. The lowest initial bed temperature considered was 25 °C, with the assumption that cooling water is available at 20 °C. While it is possible to lower the initial bed temperature below 25 °C using chilled water or refrigerant, this process would drastically increase the operating costs of the system. For the basic and modified TSA processes, the conditions that result in the lowest EAOC are initial bed temperatures of 25 °C and flue gas residence times of 16.1 and 32.5 s, respectively. Table 5 shows times for the adsorption and desorption cycles for a single bed as well as the total number of beds for the minimum EAOC scenarios of the basic and modified process. Additionally, dynamic profiles of the loading and temperature of the bed for these scenarios are presented in the Supporting Information (see Figs. S13 and S14). The breakdown of costs contributing to the minimum EAOC in each scenario is given in Table 6. For the basic process, an inlet pressure of 1.8 bar is required, and the amortized capital costs of the compressors along with the electricity and cooling water required to operate them is reflected in Table 6. For the modified process, the high residence time does not require compression of the flue gas and therefore these respective costs are not included. The EAOC for the optimal modified process configuration is about $37 million/year less expensive than the basic fixed bed

configuration, while the EAOCs for the basic and modified processes are approximately $55 million/year (+21.8%) and $18 million/year (+7.3%) higher than for the MEA system (EAOC of $252 million/year), respectively.

Table 4
Important variables for the TSA process configuration.

Variable	Value	Units
Bed length	10	[m]
Bed diameter	10	[m]
Outlet gas pressure	1.05	[bar]
Specific area for heating/cooling	53.3	[m^2/m^3]
Average bed loading at the end of the cycle	0.25	[mol/kg]
Basic TSA Process		
Inlet steam temperature	130	[°C]
Direct steam residence time	100	[s]
Modified TSA Process		
Cooling water approach ΔT	5	[°C]
Cooling water flow	175	[kg/s]
Hot water inlet temperature	130	[°C]
Hot water flow	275	[kg/s]

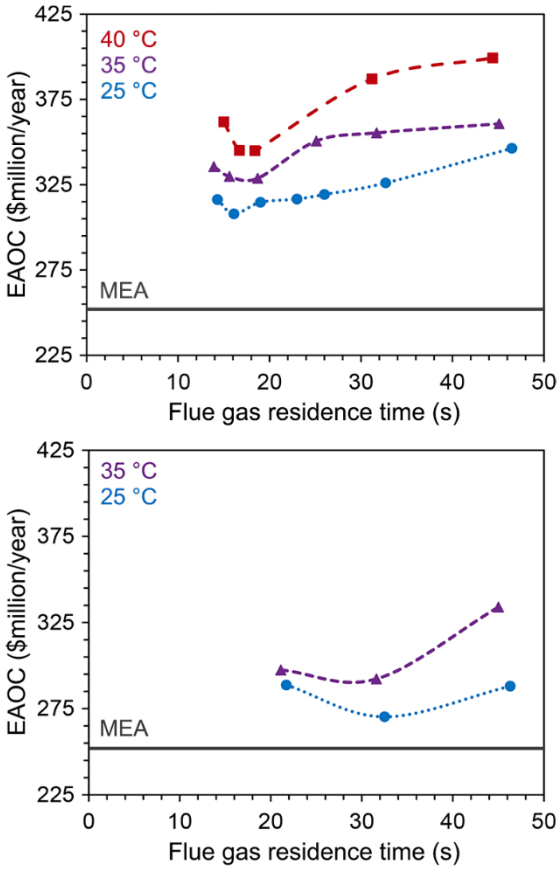

Fig. 9. Equivalent annual operating cost (EAOC) versus flue gas residence time for the basic TSA process (upper) and the modified TSA process (lower). Different colored data points indicate cost variations resulting from changing the bed temperature and flue gas temperature at the beginning of the adsorption step. Colored lines are guides for the eye. The horizontal line in both plots represents the EAOC for the state-of-the-art MEA system as discussed in the text.

Table 5
Breakdown of step times and number of beds of the optimal scenarios for the basic and modified TSA processes.

	Basic TSA Process	**Modified TSA Process**
Flue gas residence time (s)	16.1	32.5
Adsorption cycle time (s)	546	3607
Desorption cycle time (s)	1372	3551
Number of beds undergoing adsorption	12	32
Total number of beds	43	64

Table 6
Breakdown of contributing costs to the equivalent annual operating cost ($Million/year) of the optimal scenarios for the basic and modified TSA processes.

	Basic TSA Process	*Modified TSA Process*
Amortized Capital	**84.6**	**99.9**
Reactor	69.8	99.9
Compressor	14.8	–
Yearly Operating Costs	**223.2**	**170.5**
Steam	206.4	167.9
Electricity	16.4	–
Cooling Water	0.4	2.6
EAOC	**307.8**	**270.4**

3.5.2 Impact of Heat Recovery on Process Economics. During a typical TSA process, the regenerated bed contains a large amount of sensible heat that can in principle be recycled and used as a heat source elsewhere in the process (e.g., to reduce the amount of steam used for regeneration). In this section, rigorous modeling of a complicated heat recovery section is not performed, but rather the possible improvement of the process economics due to heat recovery is investigated considering two discrete values for recovery efficiencies. For a conventional MEA capture system, a lean/rich amine heat exchanger is used to extract heat from the regenerated solvent stream, with recovery efficiencies as high as 80 to 90%[32]. However, these efficiencies are not likely to feasible with a fixed bed gas–solid system as evaluated here. A practical estimate for the percent heat that could be recovered in the basic and modified TSA processes was determined based on the temperature profile in the respective beds at the end of desorption and the initial adsorption temperature. The calculated percent heat recovered varied based on the given process conditions but was found to be ~35% for the basic and modified TSA process scenarios studied here (See Section S4 of the Supporting Information). Notably, with this moderate amount of heat recovery, the estimated annual operating cost for the modified TSA process approaches that of the state-of-the-art MEA system and is approximately $26 million/year lower than the cost of the basic process (Fig. 10). In a scenario with 85% heat recovery, the modified process is only about $4 million/year less expensive than the basic process, while both processes achieve a cost savings of more than $20 million/year when compared to the MEA system (see Table S5 for EAOC breakdowns for each heat recovery case). Thus, exploring strategies to enhance and optimize heat recovery in adsorbent-based systems stands as a crucial goal toward making their process economics competitive with solvent capture systems.

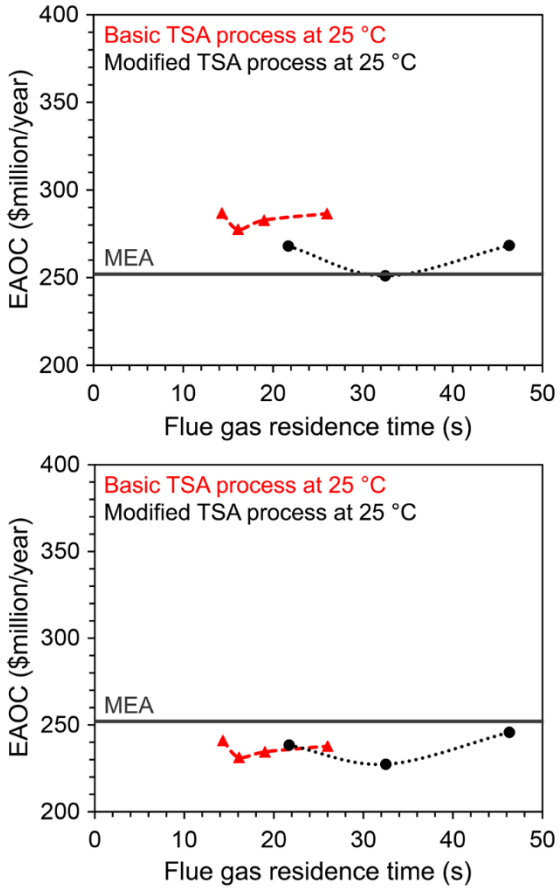

Fig. 10. EAOC versus flue gas residence time for the basic TSA process (red) and modified TSA process (black) assuming 35% practical heat recovery (upper) and 85% heat recovery (lower). The horizontal line represents the EAOC for the state-of-the-art MEA system.

3.5.3 Particle Cost Uncertainty Analysis. For the analyses completed in preceding sections of this work, the cost of the MOF particles was ignored due to a lack of accurate costing information. However, the cost of these particles will more than likely be a significant cost of the TSA process and should be accounted for. To perform this analysis, the cost of the MOF particle on a per kg basis was varied within a feasible range to investigate how the overall process economics will change. The feasible range of MOF particle costs were determined using a review performed by Liu *et al.*[33] which states that these costs can vary between 1 – 35 $/kg. The cost of zeolite 13x was estimated at $6/kg[34] and is used in this uncertainty analysis as a comparison to costs for a traditional solid sorbent. Based on the total mass of the MOF particles in the cycle and the particle cost of interest, the amortized capital cost of the particles is calculated using the same method as the other equipment as described in Eq. (41) with the life span of the MOF particles assumed to be 2 years. Fig. 11 shows the results for EAOC versus flue gas residence time with

varying MOF particle costs for the modified process with practical heat recovery. The baseline curve ($0/kg) corresponds to the results shown in Fig. 10 (upper). When a particle cost is considered that is similar to that of a traditional solid sorbent ($6/kg), process economics increase by $36 million/year (+14%) when compared to the economics when no particle cost is considered. At the upper value of the uncertainty considered in this work ($30/kg), process economics increase by $175 million/year (+70%).

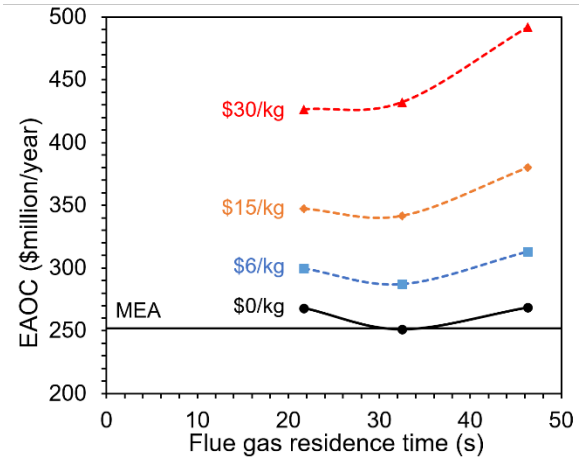

Fig. 11. EAOC versus flue gas residence time for varying costs of MOF particles ($/kg) of the modified process with practical heat recovery.

3.6 Evaluation of Energy Requirements. To further understand the techno-economic analysis results, we examined the bed temperature and loading profiles (Fig. 12) and energy requirements for the optimal basic and modified TSA process scenarios. As discussed in Section 3.4, the adsorption performance of dmpn–Mg_2(dobpdc) is highly sensitive to temperature. As seen in Fig. 12, the average bed loading for the modified process is about 130% higher than that for the basic process, due to bed cooling. The thermal energy requirements for the basic and modified processes were found to be 3.97 and 3.23 MJ/kg CO_2, respectively, calculated based on the integral steam usage and integral CO_2 captured during a single cycle, assuming the minimum EAOC scenario conditions discussed in Section 3.5.1. Note that these values are higher than the regeneration energy of 2.1 MJ/kg CO_2 reported by Milner *et al.*[8], which was calculated assuming a theoretical working capacity that is difficult to achieve in practice due to bed temperature effects discussed in this work. Regeneration energies reported for MEA systems vary in the literature. Theoretical values based on thermodynamic analysis have been reported as low as 3.4 MJ/kg CO_2[35], while process simulations of a traditional configuration have reported values as low as 3.6 MJ/kg CO_2[36]. Thus, the regeneration energy required for the modified TSA process is 19% and

10% less than that for the basic TSA and MEA processes, respectively. The lower regeneration energy required for the modified process relative to the basic process is a direct consequence of the higher loadings achieved with the former configuration (Fig. 12, lower). In particular, for modified process, a single bed remains in line longer for adsorption, decreasing the number of cycles and therefore parasitic loss associated with each cycle.

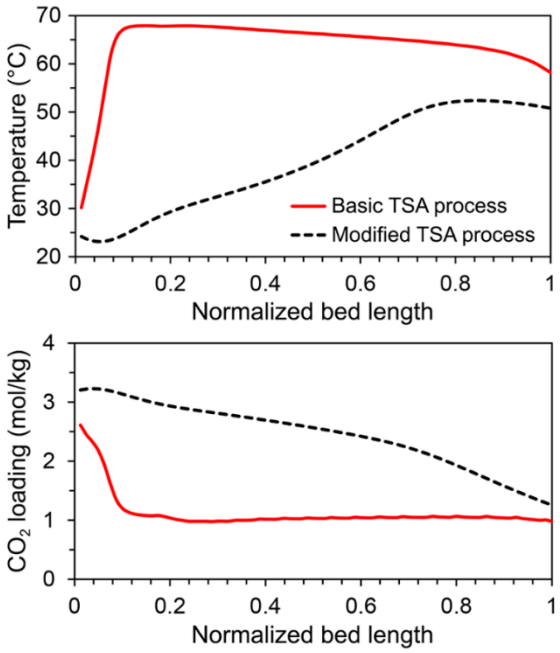

Fig. 12. Temperature (a) and loading (b) profiles at the end of the adsorption step for the basic and modified TSA processes.

4. CONCLUSIONS

In this work, a Sips isotherm model was developed that is able to accurately describe the adsorption of pure CO_2 in the metal–organic framework dmpn–Mg_2(dobpdc). The resulting parameters were also able to model validation data collected at additional temperatures that were not included in the initial parameter estimation. The kinetic model developed herein was also able to accurately describe experimental data obtained from thermogravimetric analysis. These models were developed considering adsorption of pure CO_2, which is suitable for a base case analysis given that the CO_2 adsorption capacity of dmpn–Mg_2(dobpdc) and kinetics of CO_2 adsorption in the material are not significantly affected in the presence of water. However, the development of more rigorous models will necessitate including an analysis of the effects of water co-adsorption on overall process performance.

A detailed, dynamic axial-flow fixed bed model for dmpn–Mg_2(dobpdc) was developed and validated against experimental breakthrough data. Using this model, isothermal and adiabatic systems were analyzed to investigate how temperature effects and effective heat removal will impact the adsorption performance. Our results indicate that effective removal of the heat generated during adsorption can reduce the number of adsorbent beds and subsequently the capital costs of the system by a factor of four. The fixed bed model was scaled-up to simulate two different TSA systems processing flue gas from an industrial scale power plant, one that uses condensing steam as the heating medium for regeneration (basic TSA process) and one that uses cooling water for heat removal during adsorption and hot water as well as steam for regeneration (modified TSA process). A techno-economic analysis revealed that the modified process is about $37 million/year less costly and requires 19% less energy than the basic process. These results reiterate the conclusions drawn from the isothermal and adiabatic case studies, that thermal management of this adsorbent system is a key design consideration. When factoring in a practical heat recovery of ~35%, the EAOC of the modified TSA process is further reduced by $18 million/year and approaches that of a state-of-the-art MEA capture system. Further improving heat recovery to 85% could lower the modified process EAOC by an additional $25 million/year, bringing it below that of the MEA system. An uncertainty analysis was performed to investigate the sensitivity of the total process economics to varying values of costs of the MOF particles. This study showed that the modified process EAOC would increase by a modest 14% if the cost of the MOF particles are similar to that of other solid sorbents, but economics have the possibility of increasing by nearly 70% for larger particle costs.

In this study two discrete values of heat recovery are evaluated. In reality, heat recovery can increase the cycle time due to the increase in the desorption step as a result of pre-heating the bed with a lower temperature fluid than steam as well as increase in the adsorption step as a result of pre-cooling the bed with a higher temperature fluid than the cooling water. Obviously, an increase in the cycle time might lead to higher number of beds. Furthermore, for high driving force, pre-heating a bed might need heat exchange with several beds undergoing cooling arranged in order of their temperature profile thus leading to complex operating schedule. Thus, both economic and practical considerations would be desired for setting the extent of heat recovery. Nevertheless, the results of this study highlight that the successful commercial implementation of this MOF technology will require efficient addition and rejection of heat during adsorption and desorption,

as well as heat recovery. Given the limitations of the fixed beds for heat recovery, future work will benefit from examining other types of contactor technologies, such as moving beds and rotary packed beds. The inherently better heat transfer properties of these beds will also provide better opportunities for efficient thermal management during adsorption and desorption. Due to circulating solids, those beds can reduce the amount of solids inventory, which is a critical component of the capital cost. Rigorous optimization of operating variables and contactor configuration will also serve to lower the capital and operating costs. Furthermore, this class of materials is highly tunable. Therefore, for improving the economics further, isotherm step locations and their characteristics as well as adsorption energetics can be considerably altered by varying the diamine. These aspects will be investigated in our future works.

SUPPORTING INFORMATION

- Additional isotherm modeling results
- Breakthrough time study
- Dynamic TSA profiles
- Additional heat recovery information

ACKNOWLEDGEMENTS

This research was conducted through the Carbon Capture Simulation for Industry Impact ($CCSI^2$), funded through the U.S. DOE Office of Fossil Energy by the Los Alamos National Laboratory through contract #379419. The experimental portions of the research and the contributions of R.L.S., S.T.P., S.A.D., and J.R.L. were supported by the U.S. DOE under the National Energy Technology Laboratory grant FWP-00006194. We thank Dr. Katie R. Meihaus for editorial assistance.

DISCLAIMER

manufacturer, or otherwise does not necessarily constitute or imply its endorsement, recommendation, or favoring by the United States Government or any agency thereof. The view and opinions of the authors expressed herein do not necessarily state or reflect those of the United States Government or any agency thereof.

NOTES

The authors declare the following competing financial interest(s): J.R.L. has a financial interest in Mosaic Materials, Inc., a start-up company working to commercialize metal–organic frameworks for gas separations, including CO_2 capture applications. The University of California, Berkeley has applied for a patent on some of the technology discussed herein, on which J.R.L and R.L.S. are listed as inventors.

NOMENCLATURE

A_1	Cross-sectional area pertaining to a single tube layout, [m^2]
a_p	Particle specific area, [m^2/m^3]
a_{HX}	Heat exchanger specific area, [m^2/m^3]
b_{chem}, b_{phys}	Sips isotherm parameter [bar^{-1}]
C_1	Particle diffusion parameter [$m^2/K^{0.5}/s$]
$C_{g,i}$	Concentration of species *i* in the gas phase, [mol/m^3]
$C_{p,g}$	Molar specific heat at constant pressure, [kJ/kmol/K]
$C_{p,s}$	Solids heat capacity, [kJ/kg/K]
$C_{surf,i}$	Concentration of species *i* at the particle surface, [mol/m^3]
$C_{v,g}$	Molar specific heat at constant volume, [kJ/kmol/K]
d_t	Outer diameter of heat exchanger tube, [m]
D_x	Internal diameter of reactor, [m]
D_{eff}	Effective particle diffusivity of species *i*, [m^2/s]
D_g	Molecular diffusivity of gas, [m^2/s]
d_p	Particle diameter, [m]
d_L^∞, d_B^∞, d_U^∞, d_H^∞	Weighted dual-site Langmuir isotherm parameter, [bar^{-1}]
E_{chem}	Exponential term for chemisorption reaction kinetics, [kJ/mol]
E_{phys}	Exponential term for physisorption reaction kinetics, [kJ/mol]
E_n	Sips isotherm parameter, [kJ/mol]
F_{in}	Total flow entering the bed, [mol/s]
F_{out}	Total flow leaving the bed, [mol/s]
h_f	Heat transfer coefficient between gas and particle, [$kW/m^2/K$]
h_{HX}	Fixed bed heat transfer coefficient between wall as gas, [$kW/m^2/K$]
H_{step}	Weighted dual-site Langmuir isotherm parameter, [kJ/mol]
K_a, K_c	Sips isotherm parameter, [dimensionless]
K_b, K_d	Sips isotherm parameter, [K]
k_{chem}	Chemisorption kinetic mass transfer coefficient, [1/s]
k_{phys}	Physisorption kinetic mass transfer coefficient, [1/s]
k_{eff}	Effective thermal conductivity, [kW/m/K]
k_f	External mass transfer coefficient, [m/s]
k_g	Thermal conductivity of gas, [kW/m/K]
n_{chem}, n_{phys}	Sips isotherm parameter, [dimensionless]
$n_{chem,0}$	Sips isotherm parameter, [dimensionless]
N_{chem}	Diamine loading, [mmol/g or mol/kg]
N_{phys}	Sips isotherm parameter, [mmol/g or mol/kg]
n_L, n_U	Weighted dual-site Langmuir isotherm parameter, [mmol/g or mol/kg]
n_L^∞, n_U^∞	Weighted dual-site Langmuir isotherm parameter, [mmol/g or mol/kg]
N_t	Number of heat exchanger tubes
P_g	Pressure of the gas in the bed, [bar]

p_{step}	Weighted dual-site Langmuir isotherm parameter [bar]
P_t	Heat exchanger tube pitch, [m]
q_i	Loading of species *i*, [mmol/g or mol/kg]
q_i^*	Equilibrium loading of species *i*, [mmol/g or mol/kg]
q_{chem}^{∞}	Sips isotherm parameter, [mmol/g or mol/kg]
q_{phys}^{∞}	Sips isotherm parameter, [mmol/g or mol/kg]
$Q_{st,chem}$	Sips isotherm parameter, [kJ/mol]
$Q_{st,phys}$	Sips isotherm parameter, [kJ/mol]
R	Ideal Gas Constant, [kJ/mol/K]
R_i	Mass transfer rate of component *i*, [mol/m^3/s]
t_b	Breakthrough time, [s]
T_s	Temperature of the solid phase, [K]
T_g	Temperature of the gas phase, [K]
T_0	Reference Temperature, [K]
v_g	Superficial gas velocity, [m/s]
X_1	Weighted dual-site Langmuir Isotherm parameter [K]
X_2	Weighted dual-site Langmuir Isotherm parameter [dimensionless]
z	Axial bed length [m]
y_i	Gas phase mol fraction of species *i*
ΔH_i	Heat of adsorption for species *i*, [kJ/mol]
ω	Weighted dual-site Langmuir Isotherm parameter [dimensionless]
γ	Weighted dual-site Langmuir Isotherm parameter [dimensionless]
σ	Weighted dual-site Langmuir Isotherm parameter [dimensionless]
β	Effective thermal conductivity parameter
λ	Effective thermal conductivity parameter
ε_b	Void fraction of the bed
ε_p	Porosity of the particle
ρ_g	Density of the gas, [kmol/m^3]
ρ_s	Density of the adsorbent particle, [kg/m^3]
μ_g	Viscosity of the gas, [kg/m/s]
$\propto$	Indexing placeholder
Pr	Prandtl's Number
Re	Reynold's Number
Sh	Sherwood's Number
Sc	Schmidt's Number
Nu	Nusselt's number

Common Subscripts

f	film
i	species or product
g	gas
s	solid
p	particle
$chem$	chemisorption product
$phys$	physisorption product

REFERENCES

(1) IPCC, 2014: *Climate Change 2014: Synthesis Report. Contribution of Working Groups I, II and III to the Fifth Assessment Report of the Intergovernmental Panel on Climate Change* [Core Writing Team, R.K. Pachauri and L.A. Meyer (eds.)]. IPCC, Geneva, Switzerland, 151 pp.

(2) Sumida, K.; Rogow, D. L.; Mason, J. A.; McDonald, T. M.; Bloch, E. D.; Herm, Z. R.; Bae, T.-H.; Long, J. R. Carbon Dioxide Capture in Metal–Organic Frameworks. *Chem. Rev.* **2012**, *112* (2), 724–781. https://doi.org/10.1021/cr2003272.

(3) Furukawa, H.; Cordova, K. E.; O'Keeffe, M.; Yaghi, O. M. The Chemistry and Applications of Metal-Organic Frameworks. *Science* **2013**, *341* (6149), 1230444–1230444. https://doi.org/10.1126/science.1230444.

(4) Zhou, H.-C.; Long, J. R.; Yaghi, O. M. Introduction to Metal–Organic Frameworks. *Chem. Rev.* **2012**, *112* (2), 673–674. https://doi.org/10.1021/cr300014x.

(5) McDonald, T. M.; Lee, W. R.; Mason, J. A.; Wiers, B. M.; Hong, C. S.; Long, J. R. Capture of Carbon Dioxide from Air and Flue Gas in the Alkylamine-Appended Metal–Organic Framework Mmen-Mg_2 (Dobpdc). *J. Am. Chem. Soc.* **2012**, *134* (16), 7056–7065. https://doi.org/10.1021/ja300034j.

(6) McDonald, T. M.; Mason, J. A.; Kong, X.; Bloch, E. D.; Gygi, D.; Dani, A.; Crocellà, V.; Giordanino, F.; Odoh, S. O.; Drisdell, W. S.; Vlaisavljevich, B.; Dzubak, A. L.; Poloni, R.; Schnell, S. K.; Planas, N.; Lee, K.; Pascal, T.; Wan, L. F.; Prendergast, D.; Neaton, J. B.; Smit, B.; Kortright, J. B.; Gagliardi, L.; Bordiga, S.; Reimer, J. A.; Long, J. R. Cooperative Insertion of CO_2 in Diamine-Appended Metal-Organic Frameworks. *Nature* **2015**, *519* (7543), 303–308. https://doi.org/10.1038/nature14327.

(7) Siegelman, R. L.; McDonald, T. M.; Gonzalez, M. I.; Martell, J. D.; Milner, P. J.; Mason, J. A.; Berger, A. H.; Bhown, A. S.; Long, J. R. Controlling Cooperative CO_2 Adsorption in Diamine-Appended Mg_2 (Dobpdc) Metal–Organic Frameworks. *J. Am. Chem. Soc.* **2017**, *139* (30), 10526–10538. https://doi.org/10.1021/jacs.7b05858.

(8) Milner, P. J.; Siegelman, R. L.; Forse, A. C.; Gonzalez, M. I.; Runčevski, T.; Martell, J. D.; Reimer, J. A.; Long, J. R. A Diaminopropane-Appended Metal–Organic Framework Enabling Efficient CO_2 Capture from Coal Flue Gas via a Mixed Adsorption Mechanism. *J. Am. Chem. Soc.* **2017**, *139* (38), 13541–13553. https://doi.org/10.1021/jacs.7b07612.

(9) Siegelman, R. L.; Milner, P. J.; Forse, A. C.; Lee, J.-H.; Colwell, K. A.; Neaton, J. B.; Reimer, J. A.; Weston, S. C.; Long, J. R. Water Enables Efficient CO2 Capture from Natural Gas Flue Emissions in an Oxidation-Resistant Diamine-Appended Metal–Organic Framework. *J. Am. Chem. Soc.* **2019**, *141* (33), 13171–13186. https://doi.org/10.1021/jacs.9b05567.

(10) Kim, E. J.; Siegelman, R. L.; Jiang, H. Z. H.; Forse, A. C.; Lee, J.-H.; Martell, J. D.; Milner, P. J.; Falkowski, J. M.; Neaton, J. B.; Reimer, J. A.; Weston, S. C.; Long, J. R. Cooperative Carbon Capture and Steam Regeneration with Tetraamine-Appended Metal–Organic Frameworks. *Science* **2020**, No. 369, 392–396. https://doi.org/10.1126/science.abb3976.

(11) Forse, A. C.; Milner, P. J.; Lee, J.-H.; Redfearn, H. N.; Oktawiec, J.; Siegelman, R. L.; Martell, J. D.; Dinakar, B.; Porter-Zasada, L. B.; Gonzalez, M. I.; Neaton, J. B.; Long, J.

R.; Reimer, J. A. Elucidating CO_2 Chemisorption in Diamine-Appended Metal–Organic Frameworks. *J. Am. Chem. Soc.* **2018**, *140* (51), 18016–18031. https://doi.org/10.1021/jacs.8b10203.
(12) Hefti, M.; Joss, L.; Bjelobrk, Z.; Mazzotti, M. On the Potential of Phase-Change Adsorbents for CO_2 Capture by Temperature Swing Adsorption. *Faraday Discuss.* **2016**, *192*, 153–179. https://doi.org/10.1039/C6FD00040A.
(13) Joss, L.; Hefti, M.; Bjelobrk, Z.; Mazzotti, M. On the Potential of Phase-Change Adsorbents for CO_2 Capture by Temperature Swing Adsorption. *Energy Procedia* **2017**, *114*, 2271–2278. https://doi.org/10.1016/j.egypro.2017.03.1375.
(14) Casas, N.; Schell, J.; Joss, L.; Mazzotti, M. A Parametric Study of a PSA Process for Pre-Combustion CO_2 Capture. *Separation and Purification Technology* **2013**, *104*, 183–192. https://doi.org/10.1016/j.seppur.2012.11.018.
(15) Casas, N.; Schell, J.; Pini, R.; Mazzotti, M. Fixed Bed Adsorption of CO_2/H_2 Mixtures on Activated Carbon: Experiments and Modeling. *Adsorption* **2012**, *18* (2), 143–161. https://doi.org/10.1007/s10450-012-9389-z.
(16) Pai, K. N.; Baboolal, J. D.; Sharp, D. A.; Rajendran, A. Evaluation of Diamine-Appended Metal-Organic Frameworks for Post-Combustion CO_2 Capture by Vacuum Swing Adsorption. *Sep. and Pur. Tech.* **2019**, *211*, 540–550. https://doi.org/10.1016/j.seppur.2018.10.015.
(17) Kundu, J.; Stilck, J. F.; Lee, J.-H.; Neaton, J. B.; Prendergast, D.; Whitelam, S. Cooperative Gas Adsorption without a Phase Transition in Metal-Organic Frameworks. *Phys. Rev. Lett.* **2018**, *121* (1), 015701. https://doi.org/10.1103/PhysRevLett.121.015701.
(18) Remy, T.; Baron, G. V.; Denayer, J. F. M. Modeling the Effect of Structural Changes during Dynamic Separation Processes on MOFs. *Langmuir* **2011**, *27* (21), 13064–13071. https://doi.org/10.1021/la203374a.
(19) Bao, Z.; Yu, L.; Ren, Q.; Lu, X.; Deng, S. Adsorption of CO_2 and CH_4 on a Magnesium-Based Metal Organic Framework. *Journal of Colloid and Interface Science* **2011**, *353* (2), 549–556. https://doi.org/10.1016/j.jcis.2010.09.065.
(20) Tzabar, N.; ter Brake, H. J. M. Adsorption Isotherms and Sips Models of Nitrogen, Methane, Ethane, and Propane on Commercial Activated Carbons and Polyvinylidene Chloride. *Adsorption* **2016**, *22* (7), 901–914. https://doi.org/10.1007/s10450-016-9794-9.
(21) Martell, J. D.; Milner, P. J.; Siegelman, R. L.; Long, J. R. Kinetics of Cooperative CO_2 Adsorption in Diamine-Appended Variants of the Metal–Organic Framework Mg_2 (Dobpdc). *Chem. Sci.* **2020**, *11* (25), 6457–6471. https://doi.org/10.1039/D0SC01087A.
(22) Shafeeyan, M. S.; Wan Daud, W. M. A.; Shamiri, A. A Review of Mathematical Modeling of Fixed-Bed Columns for Carbon Dioxide Adsorption. *Chemical Engineering Research and Design* **2014**, *92* (5), 961–988. https://doi.org/10.1016/j.cherd.2013.08.018.
(23) Ruthven, D. M. *Principles of Adsorption and Adsorption Processes*; John Wiley & Sons, 1984. pg. 136.
(24) Kakac, S.; Liu, H.; Pramuanjaroenkij, A. *Heat Exchangers: Selection, Rating, and Thermal Design*, 3rd ed.; CRC press, 2012. pgs. 311-367.
(25) Kim, H.; Miller, D. C.; Modekurti, S.; Omell, B.; Bhattacharyya, D.; Zitney, S. E. Mathematical Modeling of a Moving Bed Reactor for Post-Combustion CO_2 Capture. *AIChE J.* **2016**, *62* (11), 3899–3914. https://doi.org/10.1002/aic.15289.
(26) Kotamreddy, G.; Hughes, R.; Bhattacharyya, D.; Stolaroff, J.; Hornbostel, K.; Matuszewski, M.; Omell, B. Process Modeling and Techno-Economic Analysis of a CO_2

Capture Process Using Fixed Bed Reactors with a Microencapsulated Solvent. *Energy Fuels* **2019**, *33* (8), 7534–7549. https://doi.org/10.1021/acs.energyfuels.9b01255.
(27) Penny, C.; Naylor, D.; Friedman, J. Heat Transfer to Small Cylinders Immersed in a Packed Bed. *International Journal of Heat and Mass Transfer* **2010**, *53* (23–24), 5183–5189. https://doi.org/10.1016/j.ijheatmasstransfer.2010.07.042.
(28) Cavenati, S.; Grande, C. A.; Rodrigues, A. E. Separation of CH_4 / CO_2 / N_2 Mixtures by Layered Pressure Swing Adsorption for Upgrade of Natural Gas. *Chem. Eng. Sc.* **2006**, *61* (12), 3893–3906. https://doi.org/10.1016/j.ces.2006.01.023.
(29) Turton, R.; Shaeiwitz, J. A.; Bhattacharyya, D.; Whiting, W. B. *Analysis, Synthesis, and Design of Chemical Processes, Fifth Edition*; Prentice Hall, 2018. pgs. 171-212, 347-368.
(30) Plaza, M. G.; Rubiera, F.; Pevida, C. Evaluating the Feasibility of a TSA Process Based on Steam Stripping in Combination with Structured Carbon Adsorbents To Capture CO_2 from a Coal Power Plant. *Energy Fuels* **2017**, *31* (9), 9760–9775. https://doi.org/10.1021/acs.energyfuels.7b01508.
(31) Fout, T.; Zoelle, A.; Keairns, D.; Pinkerton, L. L.; Turner, M. J.; Woods, M.; Kuehn, N.; Shah, V.; Chou, V. *Cost and Performance Baseline for Fossil Energy Plants Volume 1a: Bituminous Coal (PC) and Natural Gas to Electricity Revision 3*; DOE/NETL-2015/1723, 1480987; 2015; p DOE/NETL-2015/1723, 1480987. https://doi.org/10.2172/1480987.
(32) Raksajati, A.; Ho, M. T.; Wiley, D. E. Techno-Economic Evaluation of CO_2 Capture from Flue Gases Using Encapsulated Solvent. *Ind. Eng. Chem. Res.* **2017**, *56* (6), 1604–1620. https://doi.org/10.1021/acs.iecr.6b04095.
(33) Liu, J.; Thallapally, P. K.; McGrail, B. P.; Brown, D. R.; Liu, J. Progress in Adsorption-Based CO_2 Capture by Metal–Organic Frameworks. *Chem. Soc. Rev.* **2012**, *41* (6), 2308–2322. https://doi.org/10.1039/C1CS15221A.
(34) Su, F.; Lu, C. CO_2 Capture from Gas Stream by Zeolite 13X Using a Dual-Column Temperature/Vacuum Swing Adsorption. *Energy Environ. Sci.* **2012**, *5* (10), 9021. https://doi.org/10.1039/c2ee22647b.
(35) Oyenekan, B. A. Modeling of Strippers for CO_2 Capture Using Aqueous Amines, Ph.D. Dissertation. The University of Texas at Austin, 2007.
(36) Li, K.; Cousins, A.; Yu, H.; Feron, P.; Tade, M.; Luo, W.; Chen, J. Systematic Study of Aqueous Monoethanolamine-Based CO_2 Capture Process: Model Development and Process Improvement. *Energy Sci. Eng.* **2016**, *4* (1), 23–39. https://doi.org/10.1002/ese3.101.

TOC Graphic

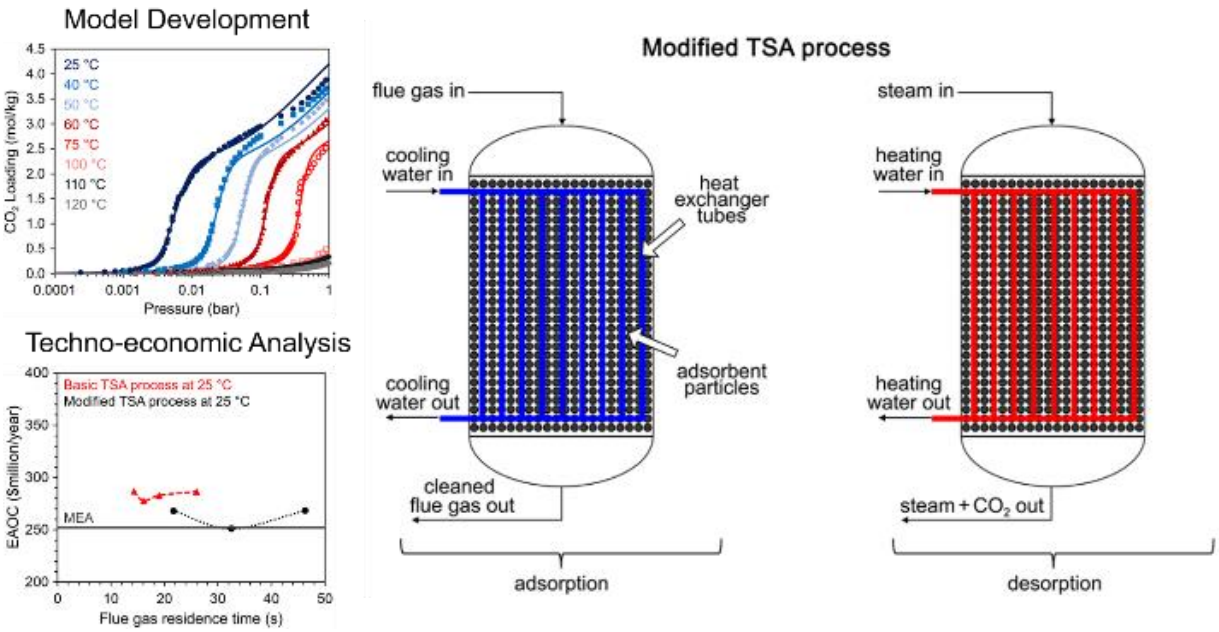
Model Development
25 °C
40 °C
50 °C
60 °C
75 °C
100 °C
110 °C
120 °C
CO2 Loading (mol/kg)
Pressure (bar)
Techno-economic Analysis
Basic TSA process at 25 °C
Modified TSA process at 25 °C
MEA
EAOC ($million/year)
Flue gas residence time (s)
Modified TSA process
flue gas in
cooling water in
heat exchanger tubes
adsorbent particles
cooling water out
cleaned flue gas out
adsorption
steam in
heating water in
heating water out
steam + CO2 out
desorption

TABLES/FIGURES

Table 1
Fixed bed reactor model constants.

Parameter	Value	Units
Heat of CO_2 Adsorption ($\Delta \boldsymbol{H_{CO_2}}$)	−65	[kJ/mol]
Adsorbent Heat Capacity ($\boldsymbol{C_{p,s}}$)	1.457	[kJ·kg^{-1}·K^{-1}]
Bed Voidage ($\boldsymbol{\varepsilon_b}$)	0.68	[m^3 void/m^3 bed]
Density of adsorbent particle ($\boldsymbol{\rho_s}$)	1000	[kg/m^3]
Particle diameter ($\boldsymbol{d_p}$)	525	[μm]
Diameter of heat exchanger tubes ($\boldsymbol{d_t}$)	1	[inches]
Heat exchanger tube pitch ($\boldsymbol{P_t}$)	0.04	[m]

Table 2
Experimental breakthrough conditions used to collect data to validate the fixed bed model.

Variable	Value	Units
Bed Length	13.34	[cm]
Bed Diameter	0.46	[cm]
Temperature	40	[°C]
Pressure	1	[bar]
Volumetric Flow Rate	10	[sccm]
y_{CO2}	0.15	[mol fraction]
y_{N2}	0.85	[mol fraction]

Table 3
Process conditions for thermal management case studies.

Variable	Value	Units
Flue Gas Pressure	1.1	[bar]
Flue Gas Temperature	25	[°C]
Flue Gas Flow rate	120	[mol/s]
Flue Gas Composition		
y_{CO2}	0.132	[mol fraction]
y_{H2O}	0.055	[mol fraction]
y_{N2}	0.813	[mol fraction]
Bed Length	10	[m]
Bed Diameter	3	[m]
Initial Bed Temperature	25	[°C]
Initial Bed Loading	0	[mol/kg]

Table 4
Important variables for the TSA process configuration.

Variable	Value	Units
Bed length	10	[m]
Bed diameter	10	[m]
Outlet gas pressure	1.05	[bar]
Specific area for heating/cooling	53.3	[m^2/m^3]
Average bed loading at the end of the cycle	0.25	[mol/kg]
Basic TSA Process		
Inlet steam temperature	130	[°C]
Direct steam residence time	100	[s]
Modified TSA Process		
Cooling water approach ΔT	5	[°C]
Cooling water flow	175	[kg/s]
Hot water inlet temperature	130	[°C]
Hot water flow	275	[kg/s]

Table 5
Breakdown of step times and number of beds of the optimal scenarios for the basic and modified TSA processes.

	Basic TSA Process	**Modified TSA Process**
Flue gas residence time (s)	14.3	32.5
Adsorption step time (s)	449	3607
Desorption step time (s)	1368	3551
Number of required adsorption beds	10	32
Total number of beds in cycle	41	64

Table 6
Breakdown of contributing costs to the equivalent annual operating cost ($Million/year) of the optimal scenarios for the basic and modified TSA processes.

	Basic TSA Process	*Modified TSA Process*
Amortized Capital	**84.6**	**99.9**
Reactor	69.8	99.9
Compressor	14.8	–
Yearly Operating Costs	**223.2**	**170.5**
Steam	206.4	167.9
Electricity	16.4	–
Cooling Water	0.4	2.6
EAOC	**307.8**	**270.4**

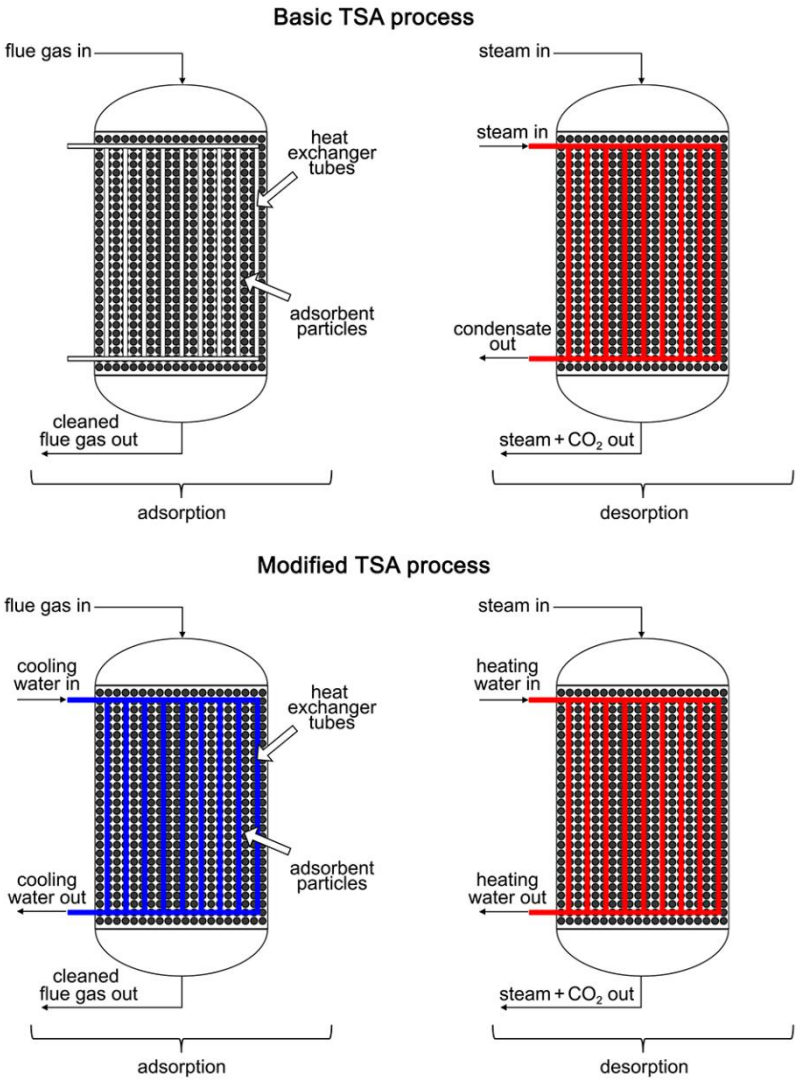

Fig. 1. Configuration steps for the basic TSA process (upper) and the modified TSA process (lower).

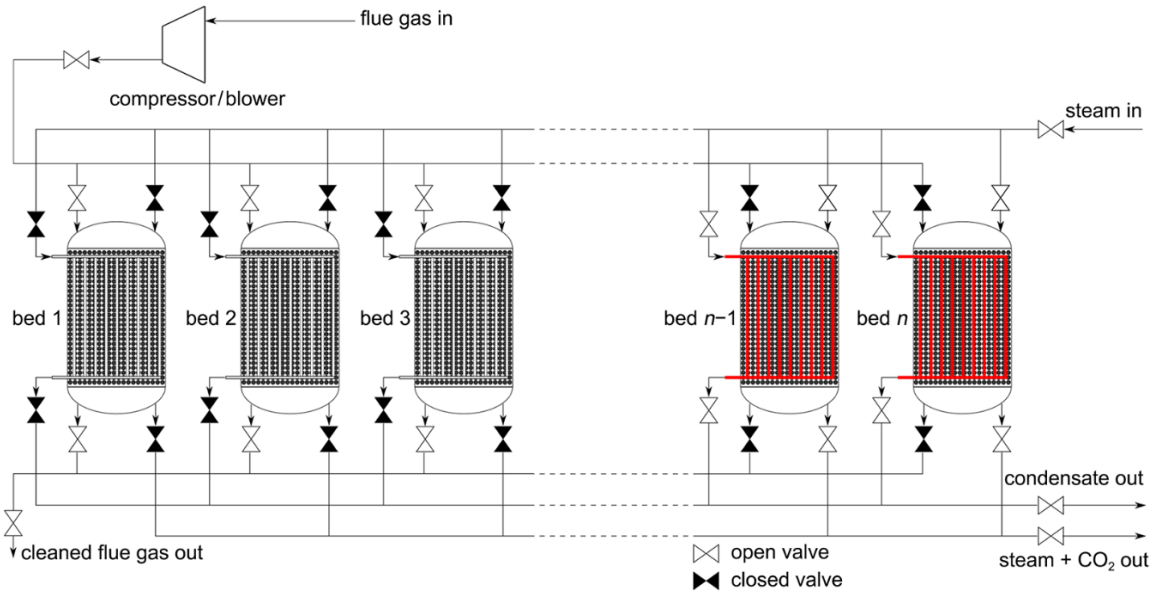

Fig. 2. Simplified diagram of the parallel bed configuration used in modeling the basic TSA cycle. A process that uses *n* beds is shown, with dashed lines representing the possibility of introducing more beds.

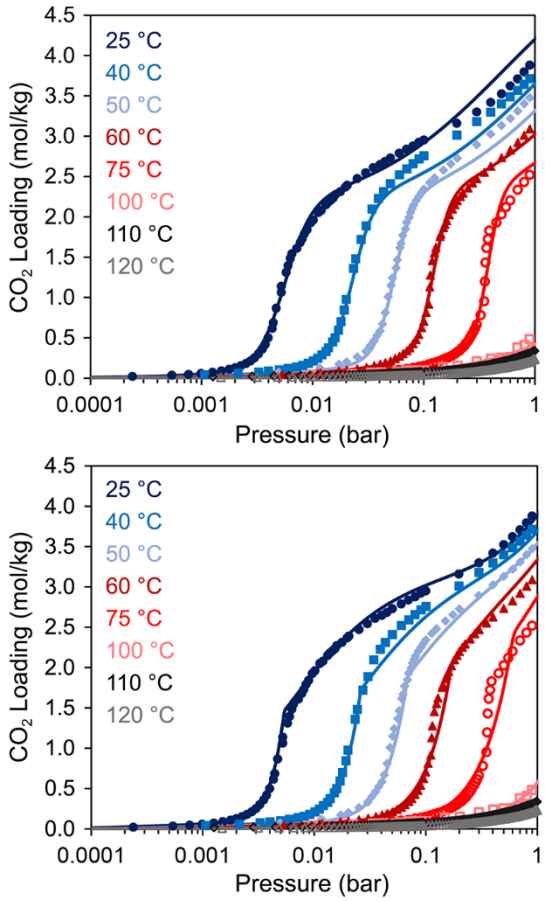

Fig. 3. Experimental CO_2 adsorption isotherms for dmpn–Mg_2(dobpdc) at the indicated temperatures (colored symbols) and fits (colored lines) using a dual-site Sips isotherm model (upper) and a weighted dual-site Langmuir isotherm model (lower).

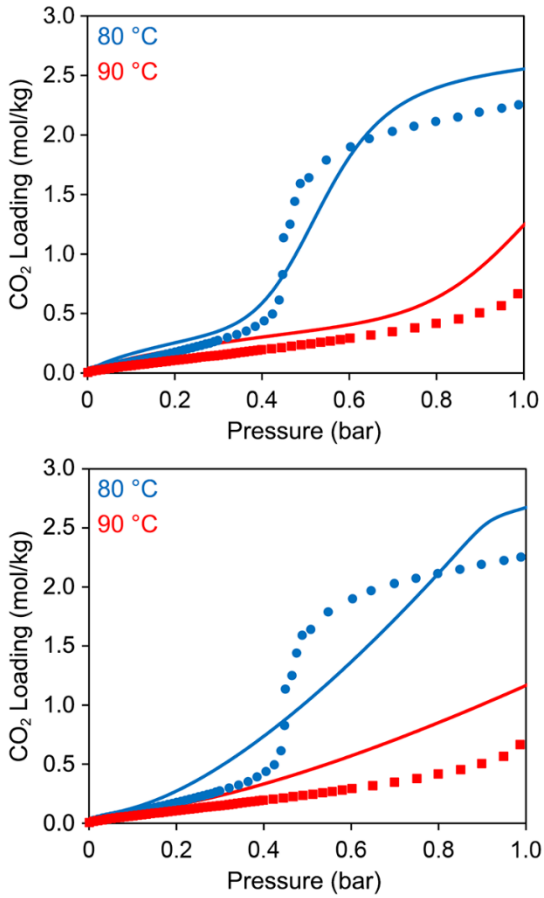

Fig. 4. Model validation results for the dual-site Sips model (upper) and weighted dual-site Langmuir model (lower). Experimental CO_2 adsorption data for dmpn–Mg_2(dobpdc) at 80 and 90 °C are shown as colored symbols and fits to the data are shown as colored lines.

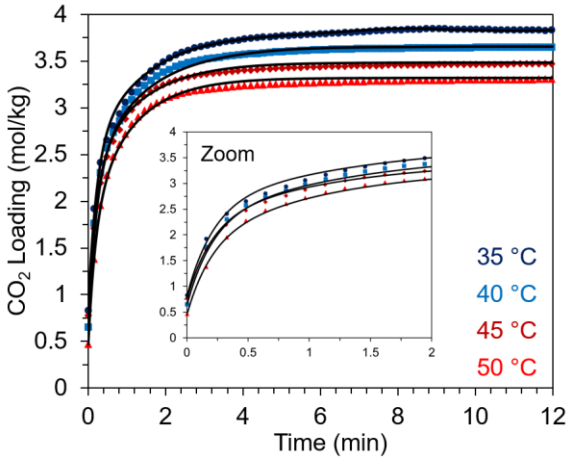

Fig. 5. Experimental data for time-dependent CO_2 adsorption in dmpn−Mg_2(dobdc) (colored symbols) and fits obtained using the linear driving force kinetic model in Section 2.2 (lines), yielding parameters $k_{chem,0}$ = 0.0136 s^{-1} / E_{chem} = 23.21 kJ/mol and $k_{phys,0}$ = 0.0823 s^{-1} / E_{chem} = 7.18 kJ/mol (root mean squared error = 0.025).

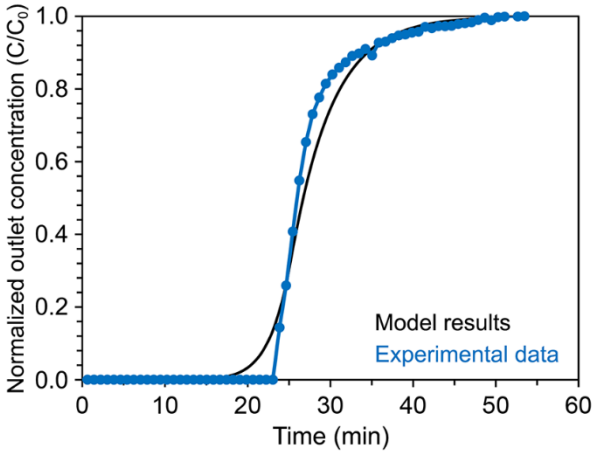

Fig. 6. Comparison of breakthrough model prediction (black trace) and experimental breakthrough data (blue trace). The normalized outlet concentration, C/C_0, represents the concentration of gas phase CO_2 exiting the bed relative to gas phase CO_2 entering the bed (root mean squared error = 0.051).

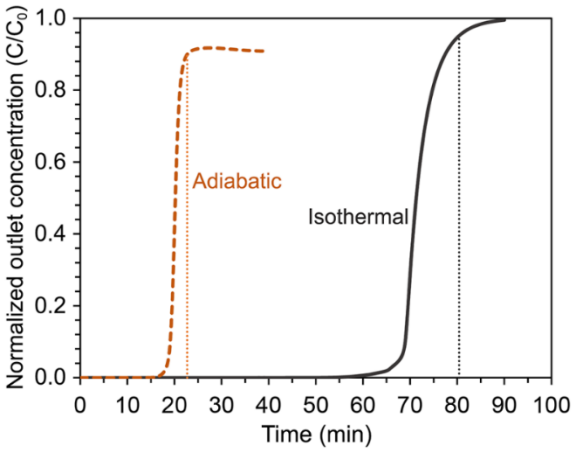

Fig. 7. Modeled breakthrough curves for isothermal and adiabatic case studies discussed in the text. The normalized outlet concentration C/C_0 represents the concentration of gas phase CO_2 exiting the bed relative to gas phase CO_2 entering the bed. Vertical lines correspond to the breakthrough times for each scenario.

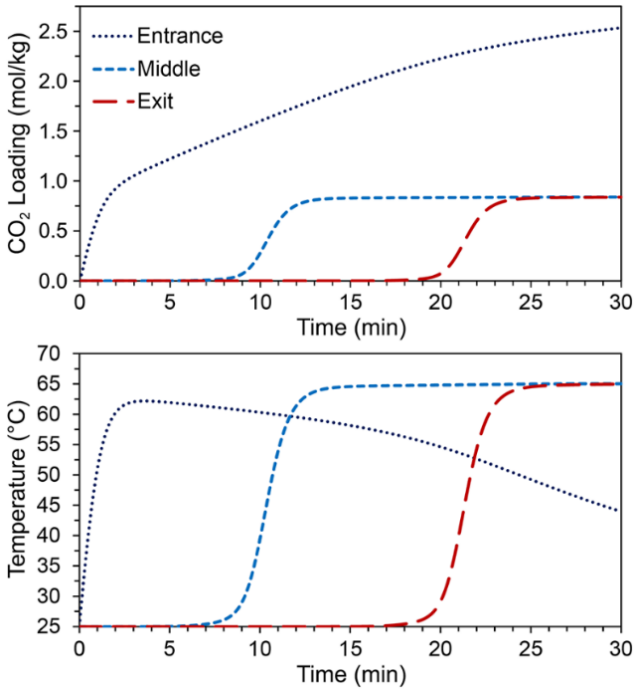

Fig. 8. Dynamic loading (upper) and temperature (lower) profiles at the entrance, middle, and exit of the bed for the adiabatic case study.

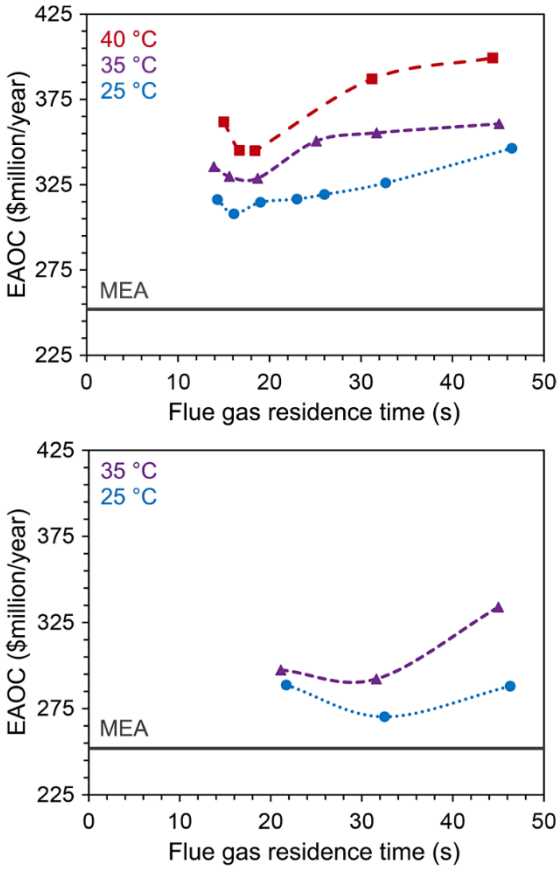

Fig. 9. Equivalent annual operating cost (EAOC) versus flue gas residence time for the basic TSA process (upper) and the modified TSA process (lower). Different colored data points indicate cost variations resulting from changing the bed temperature and flue gas temperature at the beginning of the adsorption step. Colored lines are guides for the eye. The horizontal line in both plots represents the EAOC for the state-of-the-art MEA system as discussed in the text.

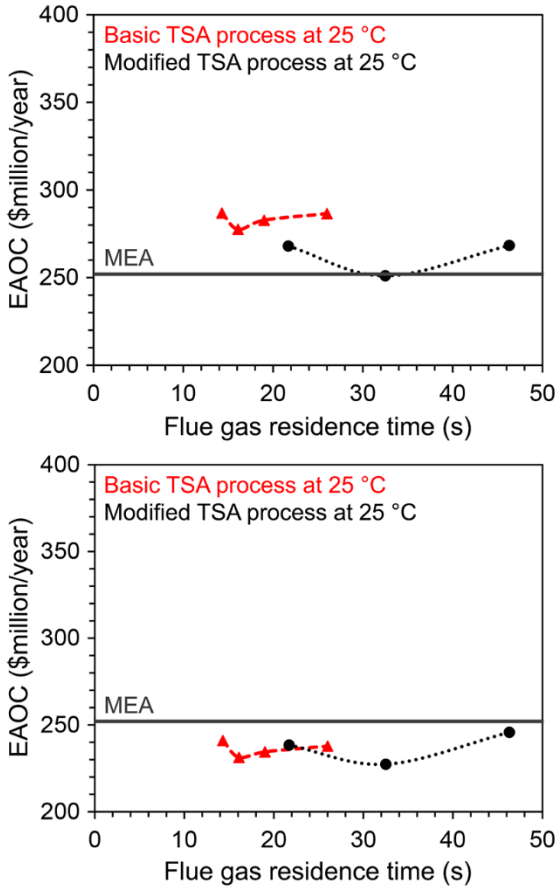

Fig. 10. EAOC versus flue gas residence time for the basic TSA process (red) and modified TSA process (black) assuming 35% practical heat recovery (upper) and 85% heat recovery (lower). The horizontal line represents the EAOC for the state-of-the-art MEA system.

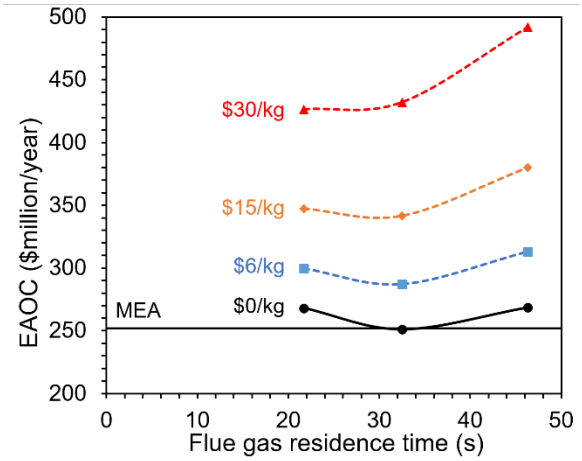

Fig. 11. EAOC versus flue gas residence time for varying costs of MOF particles ($/kg) of the modified process with practical heat recovery.

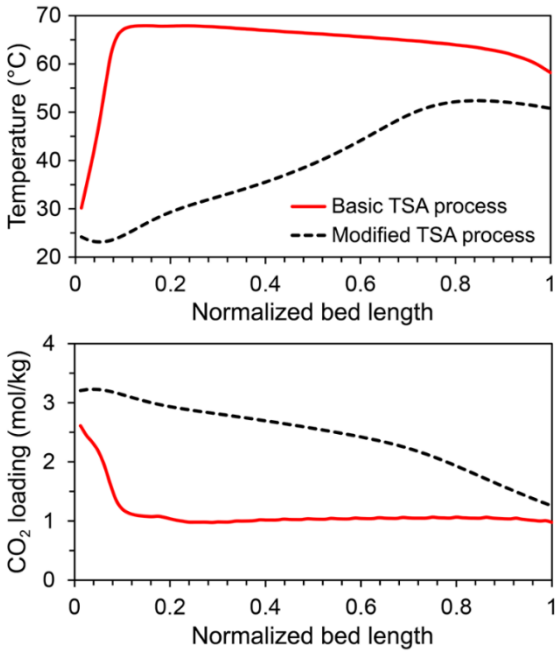

Fig. 12. Temperature (a) and loading (b) profiles at the end of the adsorption step for the basic and modified TSA processes.